



**HAL**  
open science

## Ductility limit prediction using a GTN damage model coupled with localization bifurcation analysis

Lotfi Mansouri, Hocine Chalal, Farid Abed-Meraim

► **To cite this version:**

Lotfi Mansouri, Hocine Chalal, Farid Abed-Meraim. Ductility limit prediction using a GTN damage model coupled with localization bifurcation analysis. *Mechanics of Materials*, 2014, 76, pp.64-92. 10.1016/j.mechmat.2014.06.005 . hal-01196426

**HAL Id: hal-01196426**

**<https://hal.science/hal-01196426>**

Submitted on 9 Sep 2015

**HAL** is a multi-disciplinary open access archive for the deposit and dissemination of scientific research documents, whether they are published or not. The documents may come from teaching and research institutions in France or abroad, or from public or private research centers.

L'archive ouverte pluridisciplinaire **HAL**, est destinée au dépôt et à la diffusion de documents scientifiques de niveau recherche, publiés ou non, émanant des établissements d'enseignement et de recherche français ou étrangers, des laboratoires publics ou privés.



## Science Arts & Métiers (SAM)

is an open access repository that collects the work of Arts et Métiers ParisTech researchers and makes it freely available over the web where possible.

This is an author-deposited version published in: <http://sam.ensam.eu>  
Handle ID: <http://hdl.handle.net/10985/9973>

### To cite this version :

Lotfi MANSOURI, Hocine CHALAL, Farid ABED-MERAIM - Ductility limit prediction using a GTN damage model coupled with localization bifurcation analysis - Mechanics of Materials - Vol. 76, p.64-92 - 2014

Any correspondence concerning this service should be sent to the repository

Administrator : [archiveouverte@ensam.eu](mailto:archiveouverte@ensam.eu)

## Accepted Manuscript

Ductility limit prediction using a GTN damage model coupled with localization bifurcation analysis

Lotfi Zoher Mansouri, Hocine Chalal, Farid Abed-Meraim

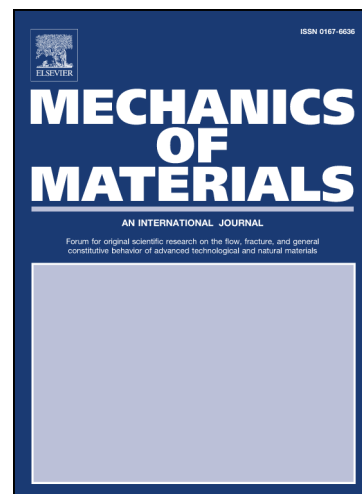
PII: S0167-6636(14)00104-5  
DOI: <http://dx.doi.org/10.1016/j.mechmat.2014.06.005>  
Reference: MECMAT 2282

To appear in: *Mechanics of Materials*

Received Date: 2 April 2014  
Revised Date: 6 June 2014

Please cite this article as: Mansouri, L.Z., Chalal, H., Abed-Meraim, F., Ductility limit prediction using a GTN damage model coupled with localization bifurcation analysis, *Mechanics of Materials* (2014), doi: <http://dx.doi.org/10.1016/j.mechmat.2014.06.005>

This is a PDF file of an unedited manuscript that has been accepted for publication. As a service to our customers we are providing this early version of the manuscript. The manuscript will undergo copyediting, typesetting, and review of the resulting proof before it is published in its final form. Please note that during the production process errors may be discovered which could affect the content, and all legal disclaimers that apply to the journal pertain.



# Ductility limit prediction using a GTN damage model coupled with localization bifurcation analysis

Lotfi Zoher MANSOURI, Hocine CHALAL, Farid ABED-MERAIM\*

LEM3, UMR CNRS 7239 – Arts et Métiers ParisTech, 4 rue Augustin Fresnel, 57078 Metz Cedex 3, France

DAMAS, Laboratory of Excellence on Design of Alloy Metals for low-mAss Structures, Université de Lorraine, France

## Abstract

Because the localization of deformation into narrow planar bands is often precursor to material failure, several approaches have been proposed to predict this phenomenon. In this paper, the Gurson–Tvergaard–Needleman (GTN) elastic–plastic–damage model for ductile materials is considered. A large-strain version of this constitutive model is coupled with the Rice localization criterion, which is based on bifurcation theory, to investigate strain localization. The resulting loss of ellipticity condition is then used to determine ellipticity loss diagrams (ELDs) associated with strain paths that are those typically applied to metals under biaxial stretching. A sensitivity analysis is conducted with respect to the model parameters on a representative selection of ductile materials. The analysis shows that the damage parameters have a significant impact on the predicted ELDs, which confirms the predominant role of damage-induced softening in triggering plastic flow localization with the adopted constitutive description combined with the bifurcation approach. As a consequence of this high sensitivity, it appears that the proper identification of damage parameters is a key issue for accurate plastic flow localization predictions using the GTN model coupled with bifurcation theory. The effect of the dense matrix hardening parameters on the strain localization predictions of the voided aggregate, although found much smaller in the whole, is more noticeable for the plane strain tension loading path or, more generally, when the critical hardening modulus required for localization is not strongly negative.

**Keywords:** Finite elasto-plasticity; Ductile GTN damage; Plastic flow localization; Rice’s bifurcation analysis; Ellipticity loss diagram

\* Corresponding author. Tel.: +(33) 3.87.37.54.79; fax: +(33) 3.87.37.54.70.

*E-mail address:* farid.abed-meraim@ensam.eu (F. Abed-Meraim).

## 1. Introduction

Commonly observed material instabilities usually manifest themselves in the form of shear bands, in three-dimensional solids, or in the form of localized necking in thin sheet metals. In the latter context, they represent one of the principal phenomena that limit sheet metal formability. To characterize the ductility of sheet metals that are subjected to forming operations, Keeler and Backofen (1963) and Goodwin (1968) proposed the use of forming limit diagrams (FLDs). This practical concept was originally based on an experimental approach involving the use of metal sheets with different geometries to reproduce a certain range of loading paths. However, the experimental approach turned out to be both expensive and time consuming. For these reasons, over the last few decades, much effort has been devoted to the development of theoretical approaches for the prediction of FLDs. For these predictions, two key components are necessary. First, a constitutive model is needed to reproduce the material response for a given loading path, and second, a localization criterion is introduced to detect the occurrence of necking instabilities.

Within the framework of classical phenomenological elastic–plastic constitutive modeling with associative plasticity and smooth yield surfaces, it has been shown (Rudnicki and Rice, 1975; Rice, 1976) that localization bifurcation into a planar band cannot occur in the hardening regime, therefore requiring softening, which may be introduced by coupling with damage. Two major damage theories have been developed in the literature during the past three decades. The first theory, known as continuum damage mechanics (see, e.g., Lemaitre, 1992; Voyiadjis and Kattan, 1999; Brünig, 2002, 2003; Menzel et al., 2005), is based on the introduction of a scalar or tensor internal variable that represents the surface density of the defects. The second theory, based on a physically motivated micromechanics approach, reproduces the kinematics of the voids (due to nucleation, growth and coalescence) within the material when it is subjected to different loading conditions. In the latter theory, the effect of the hydrostatic pressure on the material behavior is accounted for by the void volume fraction (Rice and Tracey, 1969; Gurson, 1977; Lee and Mear, 1990; Leblond et al., 1995; Gologanu et al., 1997; Monchiet et al., 2008; Tekoglu and Pardoen, 2010; Lecarme et al., 2011). In the current work, the second approach for damage modeling is adopted, and more specifically, the Gurson–Tvergaard–Needleman (GTN) model is used (see Tvergaard, 1981; Tvergaard and Needleman, 1984; Tvergaard, 1987). This model was subsequently modified to take into consideration the isotropic and kinematic hardening that is induced by plastic strain, as well as strain-path changes (see, e.g., Mear and Hutchinson, 1985; Leblond et al., 1995; Besson and Guillemer-Neel, 2003) and, more recently, plastic anisotropy (see, e.g., Benzerga and Besson, 2001; Benzerga et al., 2004a,b). However, in this work, the original GTN model (combining isotropic hardening and the von Mises yield criterion) is considered and coupled with the bifurcation analysis to emphasize the respective effects of damage and isotropic hardening on plastic flow localization predictions.

For the prediction of plastic instabilities, whatever their form (e.g., narrow shear band, diffuse or localized necking), it is necessary to couple the selected constitutive modeling with a plastic instability criterion. Several plastic instability criteria have been developed in the literature, which differ significantly in their theoretical foundations. Swift (1952) proposed an extension to biaxial loading for the Considère maximum load criterion (Considère, 1885), which was utilized to predict diffuse necking in the expansion domain of the FLD. Concurrently, Hill (1952) proposed another extension of Considère’s criterion to biaxial loading to predict localized necking. Because Hill’s criterion is only applicable to the left-hand side of the FLD, it was

combined for some time with Swift's criterion to predict a complete FLD, although the latter only predicts diffuse necking, a phenomenon that occur relatively earlier and thus less detrimental to the material formability. Within this same class of maximum-load-based criteria, Hora et al. (1996) and Mattiasson et al. (2006) suggested another extension of the Considère criterion for the prediction of localized necking by taking into consideration strain-path changes. Marciniak and Kuczynski (1967) popularized the so-called M-K model for the determination of forming limit curves by introducing an initial defect. This defect may be a pre-existing geometric imperfection in the form of either a groove of reduced thickness that is parallel to the major strain direction (Marciniak and Kuczynski, 1967) or a groove with an initial orientation that can rotate (Hutchinson et al., 1978; Zhao et al., 1996). In contrast to this imperfection theory, theoretical approaches have been developed during the last few decades that are based on bifurcation or stability theories. This class of criteria provides a sound theoretical background without the need for introducing additional user-defined parameters, which can be perceived as being arbitrarily postulated. Examples of these approaches include the contributions of Drucker (1956) and Hill (1958), which involve a necessary condition for the loss of uniqueness of the solution of the boundary value problem, often referred to as the general bifurcation condition. A local, more conservative condition for Hill's criterion, which is more commonly known as the positiveness of the second-order work, can then be derived for application to material instability problems. In a similar manner, Valanis (1989) recently suggested using a limit-point bifurcation criterion. This criterion is associated with the stationarity of the stress state and accordingly corresponds to the singularity of the elastic-plastic tangent modulus. It can be shown that within the framework of associative plasticity and small strains, Hill's and Valanis' criteria coincide. With regard to localization in the form of shear band or localized necking, Rudnicki and Rice (1975), Stören and Rice (1975) and Rice (1976) adopted the bifurcation approach to derive a necessary condition for plastic flow localization, which was also shown to correspond to the loss of ellipticity of the associated boundary value problem. Later, Bigoni and Hueckel (1991) and Neilsen and Schreyer (1993) suggested the use of a slightly more conservative criterion for the exclusion of localization bifurcation, namely the strong ellipticity condition. Using this approach, analytical formulas for the critical hardening moduli that correspond to localization have mainly been determined within the small-strain framework. Examples of these analytical derivations of the critical hardening moduli associated with the loss of strong ellipticity are included in Rizzi and Loret (1997) and Loret and Rizzi (1997a) when anisotropy originates only from the fourth-order elasticity tensor and in Loret and Rizzi (1997b) when both elasticity and plasticity are anisotropic. Similar to the above-mentioned relationship, it can be shown that within the framework of associative plasticity and small strains, the strong ellipticity condition and Rice's criterion coincide.

In the current work, a large-strain, elastic-plastic-damage GTN model is combined with Rice's bifurcation criterion within a fully three-dimensional framework to build a simulation tool, which is then applied to strain localization analysis for a representative selection of ductile materials. A similar bifurcation-based approach was used by Haddag et al. (2009), within the framework of continuum damage mechanics, whereas Franz et al. (2009a,b) adopted a micromechanics-based model in which the formation of vertices on the current points of the yield surface is a natural outcome of crystal plasticity and plays a key destabilizing role, analogous to damage-induced softening within phenomenological elastic-plastic constitutive descriptions. It is worth noting that a similar vertex-type effect was reproduced in Stören and Rice (1975) and Hutchinson and Neale (1978) by the use of a finite-strain version of the  $J_2$  deformation theory of plasticity

instead of the conventional flow theory, which allows for localization bifurcation although being in the hardening regime of phenomenological elastic–plastic constitutive models. In Besson et al. (2003), a finite element (FE) study was conducted within the GTN–Rice modeling to investigate ductile fracture under plane strain conditions. Other recent studies have adopted the FE method to numerically simulate plastic flow localization or necking (Wu et al., 2007; Sun et al., 2009; Zhang et al., 2009; Li and Buckley, 2010). However, mesh sensitivity is a well-known drawback of such FE-based strain localization analyses, which can be removed when using non-local constitutive models, such as those considered in Borg (2007) within the framework of non-local crystal plasticity, in Lele and Anand (2009) within strain-gradient viscoplasticity, or in Mroghinski et al. (2011) for porous media.

Although the GTN–Rice coupling has already been considered for the prediction of fracture in structures, no attempt has been made for the prediction of strain localization in the whole range of strain paths that are typically applied to metals under in-plane biaxial stretching. In Yamamoto (1978), localization bifurcation has been investigated for only two loading paths, namely plane strain tension and axisymmetric uniaxial tension. Because the analysis considered the original Gurson model (Gurson, 1977), and only took into account the void growth mechanism, it was found that localization bifurcation is predicted at unrealistically high strain levels, which motivated the introduction of initial imperfections in the analysis. Considering Yamamoto’s (1978) earlier conclusions regarding the unrealistically high localization strains predicted with the bifurcation approach, subsequent contributions restricted their analysis to the growth of initial imperfections, introduced in the form of material inhomogeneities, analogously to an M–K type approach. Examples of these are the works of Saje et al. (1982) and Xu and Needleman (1992), who considered the modified Gurson model and analyzed the effect of void nucleation, Tvergaard (1982), who introduced the effect of void coalescence, Pan et al. (1983), who investigated the effect of strain-rate sensitivity, Mear and Hutchinson (1985), who studied the effect of yield surface curvature with only void growth mechanism, Tvergaard (1987), who extended the former study by including the void nucleation effects, Jeong and Pan (1992), who explored the combined and interacting effects of void nucleation, yield surface curvature, and strain-rate sensitivity. Unlike these former contributions, restricted to the imperfection approach, we reconsider in the current study the bifurcation analysis with the intended purpose of addressing whether by accounting for all mechanisms of growth, nucleation, and coalescence, within the GTN damage model, we could predict localization bifurcation at reasonable strain levels, for the full range of strain paths varying from uniaxial tension to balanced biaxial tension. Then, should this be the case, another crucial goal is to undertake a parameter sensitivity study in order to determine the most influential parameters and to identify those having a key destabilizing role in triggering plastic flow localization.

The localization bifurcation analysis conducted here is fully three-dimensional, following the pioneering approach of Rudnicki and Rice (1975) (see also, e.g., Rice, 1976; Needleman and Rice, 1978; Yamamoto, 1978). In such an approach, the localization of plastic deformation into a planar band is understood as an instability in the macroscopic constitutive description of homogeneous inelastic deformation, and may therefore be used in the assessment of the constitutive theory itself. As such, this material instability is a limiting one in the sense that it has often been associated in the literature with material failure and thus viewed as a phenomenon precursor to rupture. It is also a limiting instability (see, e.g., Hill, 1962), in the sense that local initial inhomogeneities (geometric or material) may cause localization before the onset of the bifurcation discussed here; it may also be preceded by geometrical instabilities analogous to diffuse necking that is not considered in the current analysis. It should be clarified that the above described bifurcation

approach is different from the localized necking analysis in thin ductile metal sheets, in that the latter are mostly considered as two-dimensional continua, to which the plane stress assumptions are applied (see, e.g., Hill, 1952; Stören and Rice, 1975; Hutchinson and Neale, 1978). Accordingly, the results of the current study are not intended to be compared with sheet necking analyses and the associated FLDs, and whenever such a comparison is attempted, it should only be considered qualitatively. Note, however, that some contributions have investigated the three-dimensional effects on necking instabilities (e.g., Needleman and Tvergaard, 1977; Tvergaard, 1993; Petryk and Thermann, 1996; Benallal, 1998; Ito et al., 2000); while Hutchinson et al. (1978) clarified the conditions of validity of the plane stress approximations in sheet necking analysis. In virtue of the ‘intrinsic’ nature of the adopted ‘material’ instability concept, viewed as an instability in the constitutive description, a more consistent use is proposed, which consists in setting the limits to achievable ductility of metals. This is indeed what is suggested, for instance, in Needleman and Rice (1978) and Hutchinson (1979), where it is explained that the three-dimensional localization analysis, representing an actual ‘material’ instability, provides an inherent limit to material ductility regardless of the specimen dimensions (e.g., thickness) or other geometric effects. This approach, and the associated intrinsic definition of ductility limit, could be used advantageously to classify materials in terms of ductility, and thus to help design materials with improved ductility (see, e.g., Franz et al., 2009b). Indeed, whenever material parameters can be related to some underlying physical mechanisms (e.g., within micromechanics-based constitutive descriptions), determining the influence of such parameters on ductility may contribute to identifying some microrupture / microstructure–ductility relationships, which can then be used as guidelines for elaborating advanced materials with enhanced ductility, at the very early stage of the design.

This paper is organized as follows. The main constitutive equations of the GTN model are summarized in Section 2, with a short outline of their numerical implementation. Then, the Rice bifurcation criterion is developed in Section 3, and the expression of the corresponding acoustic tensor is derived in a fully three-dimensional, finite-strain framework. Section 4 reports the simulation results from the application of the GTN–Rice coupling to a selection of ductile materials taken from the literature. A parametric study is conducted to disclose the respective impact of damage and hardening parameters on the predicted localization strains. Finally, the main results are discussed in Section 5 along with some concluding remarks.

## 2. Elastic–Plastic–Damage GTN constitutive equations

The constitutive modeling described hereafter is intended to materials undergoing large deformations, and accordingly, it will be formulated in terms of rate constitutive equations. To achieve frame-invariance of the material response, objective derivatives of the tensor-valued internal variables must be used. A convenient approach, used to ensure material frame-invariance while maintaining simple forms of the constitutive equations, consists of reformulating these equations in terms of rotation-compensated variables. In what follows, the tensor quantities are described in a convenient rotating frame so that simple material time derivatives can be used in the constitutive equations. The material is assumed to be initially stress-free and homogeneous.

The GTN model, originally proposed by Gurson (1977) and subsequently extended by Tvergaard (1981) and Tvergaard and Needleman (1984), is one of the most popular damage models for the prediction of ductile fracture (Sánchez et al., 2008; Li and Karr, 2009). This model describes the evolution of a randomly distributed volume fraction of spherical voids in porous materials. The approximate macroscopic yield

criterion, initially proposed by Gurson (1977), is based on a limit analysis and described by the following relationship

$$\Phi = \left( \frac{\Sigma_{eq}}{\bar{\sigma}} \right)^2 + 2q_1 f^* \cosh \left( \frac{3}{2} q_2 \frac{\Sigma_m}{\bar{\sigma}} \right) - 1 - q_3 f^{*2} \leq 0, \quad (1)$$

where  $\Sigma_{eq} = (3\Sigma' : \Sigma'/2)^{1/2}$  is the macroscopic equivalent stress,  $\Sigma'$  and  $\Sigma_m = tr(\Sigma)/3$  are, respectively, the deviatoric and hydrostatic part of the macroscopic Cauchy stress tensor  $\Sigma$ , and  $\bar{\sigma}$  is the yield stress of the fully dense matrix. The parameters  $q_1$ ,  $q_2$  and  $q_3$  were introduced by Tvergaard (1981) to account for the void interaction effect, while  $f^*(f)$  is a function of the void volume fraction  $f$  that has been introduced by Tvergaard (1982) to model the rapid decay of the material stress carrying capacity at the final stage of coalescence. In comparison with the classical  $J_2$  criterion, two additional contributions characterize the GTN yield criterion: the hydrostatic pressure dependence from the second term on the right-hand side of Eq. (1) and the void volume fraction, which acts as an additional internal variable and induces material softening behavior at the macroscopic level. For  $f = 0$ , the classical von Mises yield surface  $F = \Sigma_{eq} - \bar{\sigma} \leq 0$  is recovered, which corresponds to elastic–plastic constitutive equations with no coupling with damage. In what follows, only isotropic hardening is considered using the Swift hardening law defined by

$$\bar{\sigma} = k \left( \varepsilon_0 + \bar{\varepsilon}^p \right)^n, \quad (2)$$

where  $(k, \varepsilon_0, n)$  and  $\bar{\varepsilon}^p$  are, respectively, the hardening parameters and the equivalent plastic strain of the fully dense matrix material.

For isotropic GTN modeling, the macroscopic plastic strain rate tensor  $\mathbf{D}^p$  and the equivalent plastic strain rate  $\dot{\bar{\varepsilon}}^p$  in the matrix material are assumed to be related by the equivalence relationship of the plastic work rate as follows:

$$(1-f) \bar{\sigma} \dot{\bar{\varepsilon}}^p = \Sigma : \mathbf{D}^p. \quad (3)$$

This relationship is exact for  $f = 0$ , which corresponds to a matrix material with no porosity, and is a reasonable approximation for porous materials with low hardening exponents (Tvergaard, 1987). The plastic strain rate is defined by the classical flow rule

$$\mathbf{D}^p = \dot{\gamma} \mathbf{V}_\Sigma, \quad (4)$$

where  $\dot{\gamma}$  is the plastic multiplier, and  $\mathbf{V}_\Sigma = \partial\Phi/\partial\Sigma$  denotes the plastic flow direction. Combining Eqs. (2)–(4), the expressions of the equivalent plastic strain rate and yield stress rate in the matrix material are obtained as follows:

$$\dot{\bar{\varepsilon}}^p = \frac{\Sigma : \mathbf{V}_\Sigma}{(1-f) \bar{\sigma}} \dot{\gamma}, \quad \dot{\bar{\sigma}} = h(\bar{\varepsilon}^p) \frac{\Sigma : \mathbf{V}_\Sigma}{(1-f) \bar{\sigma}} \dot{\gamma}, \quad (5)$$

where  $h(\bar{\varepsilon}^p) = \partial\bar{\sigma}/\partial\bar{\varepsilon}^p$  represents the plastic hardening modulus of the fully dense matrix.

Before the onset of coalescence, the evolution of porosity, with an initial value of  $f_0$ , is due to void nucleation and growth, and the porosity rate can then be partitioned as follows:

$$\dot{f} = \dot{f}_n + \dot{f}_g, \quad (6)$$

where  $\dot{f}_n$  and  $\dot{f}_g$  represent the contributions to the porosity rate from nucleation and growth, respectively. In this paper, nucleation is considered to be strain-controlled, and the corresponding evolution law is provided with the following normal distribution relationship (see Chu and Needleman, 1980):

$$\dot{f}_n = \frac{f_N}{s_N \sqrt{2\pi}} \exp \left[ -\frac{1}{2} \left( \frac{\bar{\epsilon}^p - \epsilon_N}{s_N} \right)^2 \right] \dot{\bar{\epsilon}}^p = A_N (\bar{\epsilon}^p) \dot{\bar{\epsilon}}^p, \quad (7)$$

where the nucleation-related parameters have the following physical significance:  $f_N$  represents the volume fraction of the inclusions that are likely to nucleate,  $\epsilon_N$  denotes the equivalent plastic strain for which half of the inclusions have nucleated, and  $s_N$  is the standard deviation on  $\epsilon_N$ . The porosity rate, due to growth, strongly depends on the stress triaxiality and is described by the following relationship (see, e.g., Tvergaard, 1987):

$$\dot{f}_g = (1-f) \text{tr}(\mathbf{D}^p). \quad (8)$$

In the GTN yield criterion (1), the so-called “effective” porosity  $f^*$  is intended to account for the effect of coalescence and is equal to the actual void volume fraction  $f$  as long as the latter is less than a critical porosity. This critical porosity marks the onset of the coalescence stage, which has been phenomenologically modeled by Tvergaard and Needleman (1984) to allow for final material failure at realistic values of void volume fraction:

$$f^* = f_{cr} + \delta_{GTN} (f - f_{cr}), \quad \text{with} \quad \delta_{GTN} = \begin{cases} 1 & \text{for } f \leq f_{cr}, \\ \frac{\kappa - f_{cr}}{f_R - f_{cr}} & \text{for } f_{cr} < f \leq f_R, \end{cases} \quad (9)$$

where  $f_{cr}$  represents the critical porosity,  $f_R$  is the actual void volume fraction at final fracture, and  $\kappa = f^*(f_R)$  corresponds to the maximum admissible value for the “fictitious” effective porosity. Because  $f_R$  corresponds to the complete degradation of the material (i.e.,  $\Phi = 0$ , with  $\Sigma_{eq} = 0$  and  $\Sigma_m = 0$ ), from Eq. (1), one obtains  $\kappa = f^*(f_R) = (q_1 + \sqrt{q_1^2 - q_3})/q_3$ . The empirical relationship (9) expresses that when the material enters the coalescence stage, a “new” measure of damage  $f^*$  takes effect that increases faster than the actual porosity  $f$ , considering that  $\delta_{GTN} > 1$ , which results in accelerated degradation of mechanical properties.

## 2.1 Elastic–plastic tangent modulus for the GTN model

In this subsection, the expression of the elastic–plastic tangent modulus is derived. For this, the GTN potential  $\Phi$  and the plastic multiplier  $\dot{\gamma}$  are first rewritten in the Kuhn–Tucker form

$$\Phi \leq 0, \quad \dot{\gamma} \geq 0, \quad \Phi \dot{\gamma} = 0. \quad (10)$$

This form is convenient because it reveals that there is no plastic flow (i.e.,  $\dot{\gamma} = 0$ ) when  $\dot{\Phi} < 0$ , while a strict plastic loading (i.e.,  $\dot{\gamma} > 0$ ) necessarily implies that  $\dot{\Phi} = 0$ . The latter represents the consistency condition, and can be developed as follows:

$$\dot{\Phi} = \mathbf{V}_{\Sigma} : \dot{\Sigma} + V_{\bar{\sigma}} \dot{\bar{\sigma}} + V_{f^*} \dot{f}^* = 0, \quad (11)$$

where

$$\begin{cases} \mathbf{V}_{\Sigma} = \frac{\partial \Phi}{\partial \Sigma} = \frac{1}{\bar{\sigma}} \left[ 3 \frac{\Sigma'}{\bar{\sigma}} + q_1 q_2 f^* \sinh \left( \frac{3}{2} q_2 \frac{\Sigma_m}{\bar{\sigma}} \right) \mathbf{1} \right] \\ V_{\bar{\sigma}} = \frac{\partial \Phi}{\partial \bar{\sigma}} = -\frac{1}{\bar{\sigma}} \left[ 2 \left( \frac{\Sigma_{eq}}{\bar{\sigma}} \right)^2 + 3 q_1 q_2 f^* \frac{\Sigma_m}{\bar{\sigma}} \sinh \left( \frac{3}{2} q_2 \frac{\Sigma_m}{\bar{\sigma}} \right) \right], \\ V_{f^*} = \frac{\partial \Phi}{\partial f^*} = 2 q_1 \cosh \left( \frac{3}{2} q_2 \frac{\Sigma_m}{\bar{\sigma}} \right) - 2 q_3 f^* \end{cases} \quad (12)$$

and  $\mathbf{1}$  denotes the second-order unit tensor.

As previously mentioned, a co-rotational approach that is based on the Jaumann objective rate is used in this work. This approach is consistent with the built-in formulation in Abaqus/ Standard, where the current constitutive equations have been implemented. The stress rate is described with a hypoelastic law in the co-rotational frame via the material time derivative

$$\dot{\Sigma} = \mathbf{C}^e : (\mathbf{D} - \dot{\gamma} \mathbf{V}_{\Sigma}) = \mathbf{C}^{ep} : \mathbf{D}, \quad (13)$$

where  $\mathbf{C}^e$  denotes the fourth-order tensor of the elastic constants,  $\mathbf{C}^{ep}$  stands for the elastic–plastic tangent modulus to be determined, and the strain rate tensor  $\mathbf{D}$  is additively decomposed into its elastic and plastic parts. Substituting Eqs. (4)–(9) and (13) into the consistency condition (11), the expression of the plastic multiplier is derived as follows:

$$\dot{\gamma} = \frac{\mathbf{V}_{\Sigma} : \mathbf{C}^e : \mathbf{D}}{H_{\gamma}}, \quad (14)$$

where the scalar variable  $H_{\gamma}$  is given by

$$H_{\gamma} = \mathbf{V}_{\Sigma} : \mathbf{C}^e : \mathbf{V}_{\Sigma} - \frac{V_{\sigma h}}{(1-f)} \frac{\Sigma : \mathbf{V}_{\Sigma}}{\bar{\sigma}} - V_{f^*} \delta_{GTN} \left[ \frac{A_n}{(1-f)} \frac{\Sigma : \mathbf{V}_{\Sigma}}{\bar{\sigma}} + (1-f) \mathbf{V}_{\Sigma} : \mathbf{1} \right]. \quad (15)$$

Substituting Eq. (14) into Eq. (13) provides the expression of the elastic–plastic tangent modulus that corresponds to the GTN model:

$$\mathbf{C}^{ep} = \mathbf{C}^e - \alpha \frac{(\mathbf{C}^e : \mathbf{V}_{\Sigma}) \otimes (\mathbf{V}_{\Sigma} : \mathbf{C}^e)}{H_{\gamma}}, \quad (16)$$

where  $\alpha = 0$  for elastic loading or unloading, and  $\alpha = 1$  for strict plastic loading.

It is interesting to notice that when  $f = 0$ , these equations simplify to the classical von Mises elastic–plastic constitutive equations with isotropic hardening and no coupling with damage. These features of the model will be taken advantage of later to qualitatively validate its numerical implementation and to assess its robustness for these limiting cases of vanishing damage-related parameters.

## 2.2 Numerical implementation of the constitutive equations

This subsection briefly outlines the time integration of the GTN constitutive equations and their implementation into the static implicit FE code Abaqus/Standard. In this process, a user material (UMAT) subroutine (with a stress and state update algorithm that is developed along with the associated consistent tangent modulus) is built. In this FE context, at each equilibrium iteration, certain necessary preliminary steps (e.g., calculation of the strain increments at each integration point from the predicted nodal displacement increments), as well as subsequent steps (e.g., verification of equilibrium equations), are addressed by the FE code; therefore, our focus will be restricted to the integration of the constitutive equations over a time increment.

More specifically, this integration consists of determining the state of stress and internal variables at time  $t_{n+1}$  when starting from a known state at time  $t_n$  and a given strain increment  $\Delta\boldsymbol{\epsilon}$ . In a static implicit code, such as Abaqus/Standard, in which the equilibrium equations are solved with an implicit scheme, the consistent tangent modulus is also required to achieve the equilibrium state at the end of each loading increment. From the evolution equations that were reported in the previous section, it can be shown that the set of variables in the GTN model is governed by a general differential equation of the form

$$\dot{\mathbf{x}} = \mathbf{h}_{\mathbf{x}}(\mathbf{x}), \quad (17)$$

where vector  $\mathbf{x}$  incorporates all of the model variables (see Eqs. (4)–(8) and (13)–(14)). This general form of differential equation can encompass various hardening descriptions and more advanced yield surfaces to account for initial and induced anisotropy; however, because the current contribution focuses primarily on the impact of the damage parameters on the ductility limits set by plastic flow localization, a simple von Mises yield criterion and Swift's isotropic hardening model are considered. In the same spirit, for the applications in mind, a simple explicit time integration scheme is adopted to update the stresses and state variables of the GTN model. This choice is motivated by a reasonable compromise in terms of efficiency, accuracy and convergence. These important aspects have been widely investigated in the literature (see, e.g., Kim et al., 2008; Sánchez et al., 2008; Becker, 2011), and the respective benefits and drawbacks of various implicit and explicit time integration schemes with regard to accuracy, stability, robustness and efficiency have been discussed by many authors. Using an explicit time integration scheme, the rate equations, formally written in the compact form in Eq. (17), are integrated for each strain increment in the co-rotational frame by successively calculating the following sub-increments:

$$\Delta\mathbf{x}_0 = \mathbf{0}, \quad \Delta\mathbf{x}_i = \mathbf{h}_{\mathbf{x}}(\mathbf{x}_n + a_i\Delta\mathbf{x}_{i-1}), \quad i = 1, \dots, N, \quad (18)$$

and then explicitly updating the unknown vector  $\mathbf{x}$  as follows:

$$\mathbf{x}_{n+1} = \mathbf{x}_n + \sum_{i=1}^N b_i\Delta\mathbf{x}_i, \quad (19)$$

where  $N$  is the order of the selected explicit scheme ( $N = 4$  for the fourth-order Runge–Kutta scheme adopted here), and coefficients  $a_i$  and  $b_i$  are dependent on the chosen scheme.

To enable the FE code to solve the equilibrium equations based on an iterative procedure, the algorithmic tangent modulus, consistent with the selected time integration scheme, also needs to be determined. This

consistent tangent modulus provides the variation of the stress increment due to the variation of the strain increment, i.e.,  $D(\Delta\Sigma) = \mathbf{C}^{alg} : D(\Delta\epsilon)$ .

Combining Eqs. (18, 19) with Eqs. (13)–(16), the consistent tangent modulus is obtained as

$$\mathbf{C}^{alg} = \sum_{i=1}^N b_i \mathbf{C}^{ep}|_i, \quad \text{with} \quad \mathbf{C}^{ep}|_i = \mathbf{C}^e - \alpha \frac{(\mathbf{C}^e : \mathbf{V}_{\Sigma}|_i) \otimes (\mathbf{V}_{\Sigma}|_i : \mathbf{C}^e)}{H_{\gamma}|_i}. \quad (20)$$

### 2.3 Validation of the state update algorithm and its implementation

In this subsection, certain preliminary simulations are performed to evaluate the performance of the state update algorithm and its implementation via a UMAT subroutine in Abaqus/Standard. As stated before, the choice of using an explicit scheme is motivated by the intended applications of this study (i.e., ductility limits depicted by ellipticity loss diagrams (ELDs)), which involve considering a single material point to which are prescribed various linear loading paths that are typically applied to metals under in-plane biaxial stretching (i.e., ranging from uniaxial tension to balanced biaxial tension). In these circumstances, an explicit scheme is easier to develop and implement but requires the use of smaller loading increments. Note that the GTN model available in Abaqus/Standard is restricted to growth and nucleation mechanisms; its extension to the coalescence stage is only available in Abaqus/Explicit. The latter being primarily intended to solve dynamic, rather than quasi-static, equilibrium equations, this has motivated in part our own implementation of the full GTN model in Abaqus/Standard, to be consistent with our subsequent quasi-static bifurcation analyses.

The first simulation is specifically intended to estimate the typical size of increments that guarantees an accuracy that is comparable to that yielded by an implicit scheme. Fig. 1 compares the uniaxial tensile results from the explicit UMAT subroutine with different loading increment sizes to the reference solution from Abaqus/Standard. The latter is obtained with an implicit time integration scheme that allows for much larger loading increments (see, e.g., Haddag et al., 2007). The material parameters used in this simulation are similar to those of an Al5182 aluminum alloy (Brunet et al., 1998). Because the modified GTN model, available in Abaqus/Standard, does not allow for the coalescence stage, the original Al5182 aluminum alloy parameters have been altered by increasing the parameter  $f_{cr}$  so that coalescence is never reached. Accordingly, the resulting parameters are  $E = 70,000$  MPa and  $\nu = 0.33$  for the Young modulus and the Poisson ratio, respectively;  $k = 371.2$  MPa,  $\epsilon_0 = 0.00324$  and  $n = 0.17$  for the Swift hardening coefficients; and  $f_0 = 0.001$ ,  $s_N = 0.1$ ,  $\epsilon_N = 0.27$ ,  $f_N = 0.25$ ,  $f_{cr} = 0.5$ ,  $f_R = 0.6$ ,  $q_1 = 1.5$ ,  $q_2 = 1.0$  and  $q_3 = 2.15$  for the GTN damage parameters. Based on this set of parameters, Fig. 1 exhibits the softening regime typical of the GTN model and suggests that the size of strain increments should be maintained lower than  $10^{-5}$  to maintain the necessary accuracy, afforded by implicit schemes, up to strain levels that are sufficiently large and typical of those associated with material instabilities.

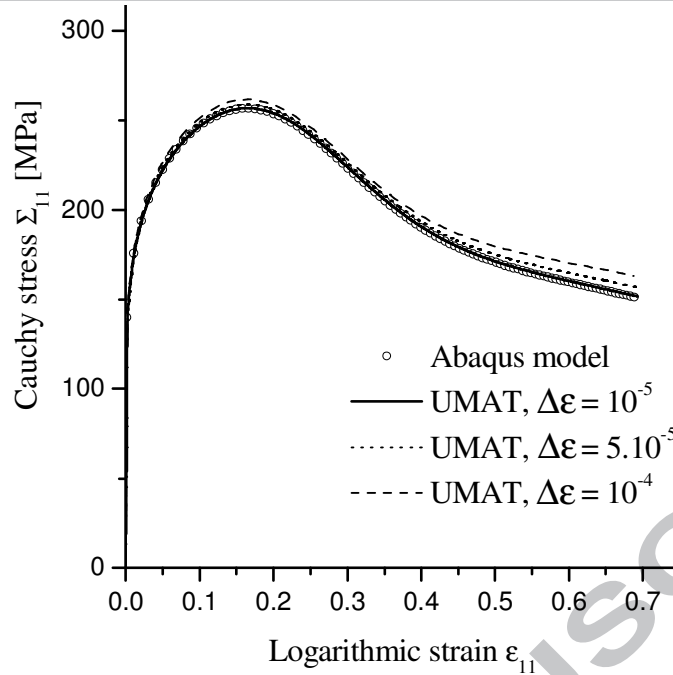


**Fig. 1.** Comparison between the Abaqus model (implicit time integration scheme) and the developed explicit UMAT subroutine (using three different-sized strain increments) for a uniaxial tensile test performed on a material similar to the Al5182 aluminum alloy.

Another series of simulations is specifically intended to qualitatively validate the numerical implementation and to assess its robustness for various values of damage parameters. As discussed in subsection 2.1, an undamaged elastic–plastic model with isotropic hardening is recovered in the limit of vanishing damage parameters (i.e., when  $A_n \rightarrow 0$ ). Considering the expression of  $A_n$  in Eq. (7), there are three different ways for  $A_n \rightarrow 0$ : either  $f_N \rightarrow 0$ ,  $\varepsilon_N \rightarrow +\infty$ , or  $s_N \rightarrow +\infty$ . Fig. 2 illustrates this limit by comparing the uniaxial tensile results from the elastic–plastic model with Swift’s isotropic hardening that is available in Abaqus/Standard to the simulations from the developed UMAT, while varying parameters  $f_N$ ,  $\varepsilon_N$  and  $s_N$ . For each of these simulations, only one of the parameters ( $f_N$ ,  $\varepsilon_N$  or  $s_N$ ) is varied at a time, starting from an initial set of parameters given by:  $E = 70,000$  MPa,  $\nu = 0.33$ ,  $k = 371.2$  MPa,  $\varepsilon_0 = 0.00324$ ,  $n = 0.17$ ,  $f_0 = 0$ ,  $s_N = 0.1$ ,  $\varepsilon_N = 0.27$ ,  $f_N = 0.35$ ,  $f_{cr} = 0.5$ ,  $f_R = 0.6$ ,  $q_1 = 1.5$ ,  $q_2 = 1$  and  $q_3 = 2.15$ .

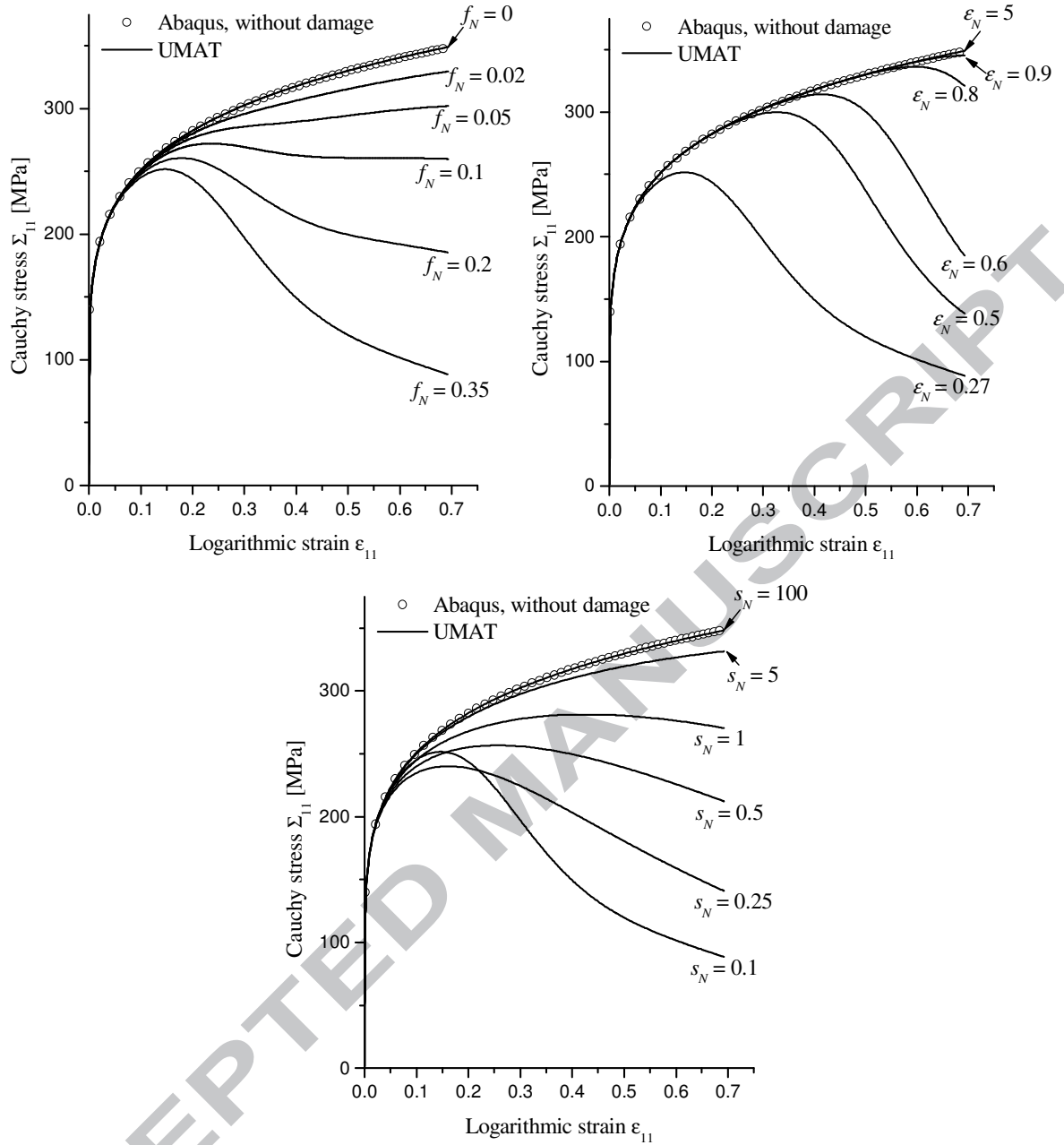


**Fig. 2.** Validation of the numerical implementation with respect to the built-in Abaqus model. An undamaged, isotropic hardening elastic–plastic model is recovered for small values of  $f_N$ , large values of  $\epsilon_N$ , or large values of  $s_N$ .

### 3. Material instability criterion

In this section, the Rudnicki and Rice material instability theory is briefly outlined (see Rudnicki and Rice, 1975; Rice, 1976), and the relevant tangent moduli necessary to build the corresponding acoustic tensor are derived. This approach is based on a bifurcation analysis, which involves loss of uniqueness for the solution of the rate equilibrium equations, with a bifurcation mode in the form of an infinite localized band. In other words, this bifurcation is interpreted as the possibility of the occurrence of a non-homogeneous strain mode

within a continuous medium that is subjected to a homogeneous strain state. Concurrently, other contributions revealed that this corresponds to the loss of ellipticity of the partial differential equations governing the associated boundary value problem. The mode of bifurcation in this approach is sought as a narrow planar localization band, defined by its normal  $\mathbf{n}$ , as illustrated in Fig. 3. The velocity gradients inside and outside the band are designated as  $\mathbf{G}^-$  and  $\mathbf{G}^+$ , respectively, while the corresponding nominal stresses are denoted as  $\mathbf{N}^-$  and  $\mathbf{N}^+$ .

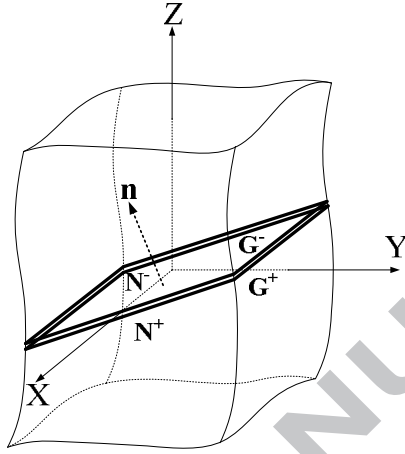


**Fig. 3.** Schematic representation of a localization band embedded in an infinite medium.

The work-conjugate variables appropriate to a bifurcation analysis within the large-strain framework are the nominal stress and velocity gradient; therefore, the constitutive equations are worked out such that Eq. (13) is substituted by its counterpart in terms of  $\mathbf{N}$  and  $\mathbf{G}$  as

$$\dot{\mathbf{N}} = \mathbf{L} : \mathbf{G}, \quad (21)$$

where  $\mathbf{L}$  represents a fourth-order constitutive tensor that needs to be determined. If we consider that the solid remains homogeneous until the onset of bifurcation (i.e., incipience of a localization band), then it is possible to derive a localization condition using the equilibrium and compatibility conditions. The stress equilibrium along the localized band, also interpreted as the normal continuity of the stress rate vector through the discontinuity surface, reads

$$\mathbf{n} \cdot \llbracket \dot{\mathbf{N}} \rrbracket = \mathbf{0}, \quad (22)$$

where  $\llbracket \cdot \rrbracket$  designates the jump in a given quantity (e.g.,  $\llbracket \dot{\mathbf{N}} \rrbracket = \dot{\mathbf{N}}^+ - \dot{\mathbf{N}}^-$  is the jump in the nominal stress rate across the discontinuity plane of normal  $\mathbf{n}$ ). In addition, the occurrence of a localization band gives rise to a jump in the velocity gradient across this band. Maxwell's compatibility condition states that this discontinuity must necessarily be in the form

$$\llbracket \mathbf{G} \rrbracket = \boldsymbol{\lambda} \otimes \mathbf{n}, \quad (23)$$

where vector  $\boldsymbol{\lambda} = \llbracket \mathbf{G} \rrbracket \cdot \mathbf{n}$  defines the localization mode (e.g., shear mode when  $\boldsymbol{\lambda} \perp \mathbf{n}$ ), which must be non-zero for effective bifurcation. Combining Eqs. (21)–(23) yields the linear system:

$$(\mathbf{n} \cdot \mathbf{L} \cdot \mathbf{n}) \cdot \boldsymbol{\lambda} = \mathbf{0}. \quad (24)$$

Finally, a necessary condition for the localization of the plastic flow into a planar localized band results from the above eigenvalue problem and is simply given by

$$\det \mathbf{Q} = \det (\mathbf{n} \cdot \mathbf{L} \cdot \mathbf{n}) = 0, \quad (25)$$

where  $\mathbf{Q}$  is the so-called acoustic tensor, the singularity of which (i.e., vanishing of its determinant) will be used as an indicator of plastic strain localization.

To proceed further, the expression of the fourth-order tensor  $\mathbf{L}$ , which has been left aside thus far, will be derived. To this end, the large-strain hypoelastic law expressed in Eq. (13) in a (material) co-rotational frame is rewritten in a fixed frame as

$$\boldsymbol{\Sigma}^\nabla = \mathbf{C}^e : (\mathbf{D} - \mathbf{D}^p), \quad (26)$$

where  $\boldsymbol{\Sigma}^\nabla$  denotes the Jaumann derivative of the Cauchy stress tensor, defined as

$$\boldsymbol{\Sigma}^\nabla = \dot{\boldsymbol{\Sigma}} - \mathbf{W} \cdot \boldsymbol{\Sigma} + \boldsymbol{\Sigma} \cdot \mathbf{W}, \quad (27)$$

where  $\mathbf{W}$  is the spin tensor (i.e., the skew-symmetric part of  $\mathbf{G} = \dot{\mathbf{F}} \cdot \mathbf{F}^{-1}$ , with  $\mathbf{F}$  the deformation gradient).

Because the nominal and Cauchy stress tensors are related to each other by the classical relationship  $\mathbf{N} = J\mathbf{F}^{-1} \cdot \boldsymbol{\Sigma}$ , where  $J = \det \mathbf{F}$ , the relationship between their rates is

$$\dot{\mathbf{N}} = J\mathbf{F}^{-1} \cdot (\dot{\boldsymbol{\Sigma}} + tr(\mathbf{D})\boldsymbol{\Sigma} - \mathbf{G} \cdot \boldsymbol{\Sigma}), \quad (28)$$

which can be further simplified in an updated Lagrangian approach that is adopted hereafter.

Finally, the combination of Eqs. (26)–(28) provides the expression of the constitutive law in terms of the nominal stress rate

$$\dot{\mathbf{N}} = \mathbf{C}^e : (\mathbf{D} - \mathbf{D}^p) + tr(\mathbf{D})\boldsymbol{\Sigma} - \mathbf{D} \cdot \boldsymbol{\Sigma} - \boldsymbol{\Sigma} \cdot \mathbf{W}. \quad (29)$$

To achieve the form of Eq. (21), each of the four terms on the right-hand side of Eq. (29) is manipulated so that the following expressions are derived:

$$\left\{ \begin{array}{l} \mathbf{C}^e : (\mathbf{D} - \mathbf{D}^p) = \mathbf{C}^{ep} : \mathbf{G} \\ tr(\mathbf{D})\boldsymbol{\Sigma} = \mathbf{C}_1 : \mathbf{G} \\ \mathbf{D} \cdot \boldsymbol{\Sigma} = \mathbf{C}_2 : \mathbf{G} \\ \boldsymbol{\Sigma} \cdot \mathbf{W} = \mathbf{C}_3 : \mathbf{G} \end{array} \right. , \quad \text{with} \quad \left\{ \begin{array}{l} \mathbf{C}_{1ijkl} = \Sigma_{ij} \delta_{kl} \\ \mathbf{C}_{2ijkl} = \frac{1}{2} (\delta_{ik} \Sigma_{jl} + \delta_{il} \Sigma_{jk}) \\ \mathbf{C}_{3ijkl} = \frac{1}{2} (\Sigma_{ik} \delta_{jl} - \Sigma_{il} \delta_{jk}) \end{array} \right. \quad (30)$$

Finally, the fourth-order constitutive tensor in Eq. (21), which is the key component in the construction of the acoustic tensor (see Eq. (25)), is given by

$$\mathbf{L} = \mathbf{C}^{ep} + \mathbf{C}_1 - \mathbf{C}_2 - \mathbf{C}_3. \quad (31)$$

At this stage, several worth noting observations can be made. First, although the analytical tangent modulus  $\mathbf{C}^{ep}$  possesses the minor and major symmetry, the resulting modulus  $\mathbf{L}$  has none of these symmetries due to the particular expressions of tensors  $\mathbf{C}_1$ ,  $\mathbf{C}_2$  and  $\mathbf{C}_3$ . Additionally, the latter fourth-order tensors, which only depend on the stress components and will be referred to in what follows as the convective

stress terms, originate from the large-strain framework. In a small-strain bifurcation analysis, only the analytical tangent modulus is included in the expression of the acoustic tensor, which then becomes fully symmetric. For some metallic materials, the effect of these convective stress components on the predicted localization strains may be small compared with the role of the analytical tangent modulus when the magnitude of these stress components is much smaller than that of the elasticity tensor. This statement will be further investigated through the prediction of the critical state associated with loss of ellipticity, based on the above-derived localization criterion.

In practice, the localization condition given in Eq. (25) represents a minimization problem in which the function to minimize depends only on the normal to the localization band. Inspection of the variation of the determinant of the acoustic tensor with the three-dimensional orientation of the normal to the localization band reveals a complex evolution with several local minima, so that available efficient optimization procedures cannot be used. Consequently, in this study, the global minimum is determined by systematically scanning the entire range of possible orientations of the normal  $\mathbf{n}$  (see, e.g., Haddag et al., 2009).

#### 4. Simulation results and discussion

In the previous sections, the GTN model was described in detail along with its coupling with the Rice localization criterion. In this section, the resulting coupling will be applied to a selection of ductile materials to investigate the occurrence of strain localization and, more specifically, the respective impact of the damage mechanisms and the dense matrix hardening parameters on the predicted limit strains.

##### 4.1 *Materials selection and associated parameters*

The application of elastic–plastic–damage models to strain localization predictions is restricted by the availability of the damage model parameters, along with experimental measures of ductility limits or other data characterizing the material state at the onset of strain localization. In this paper we use a set of material data published by Brunet and co-workers (Brunet et al., 1998; Mguil, 1997). These are steels and aluminum alloys, typically used in the metal forming industry. One steel and three aluminum alloys were tested by Brunet et al. (1998) and the associated GTN model parameters were identified. Similar data is available in Mguil (1997) for two additional steels. The corresponding material parameters, obtained from the above references, are reported in Tables 1 and 2. Parameter  $q_3$  is taken to be equal to  $q_1^2$  in many references; in this study, this value is slightly modified (i.e.,  $q_3 = 2.15$  rather than 2.25) to allow for the singularity of the acoustic tensor for certain loading paths in the positive biaxial stretching domain (e.g., in the neighborhood of balanced biaxial tension).

**Table 1**

Elastic properties and Swift's hardening parameters (pertaining to the fully dense matrix material) for the entire set of ductile materials investigated.

Material	$E$ (MPa)	$\nu$	$k$ (MPa)	$\epsilon_0$	$n$
Al5182	70,000	0.33	371.2	0.00324	0.170
Al5754	70,000	0.33	309.1	0.00173	0.177
Al6016	70,000	0.33	388.3	0.00975	0.220
Mild steel	198,000	0.3	551.1	0.00954	0.279
XES steel	198,000	0.3	551.1	0.00954	0.280
ULC/Ti	207,836	0.3	599.3	0.00352	0.260

**Table 2**

Parameters of the GTN damage model for the entire set of ductile materials investigated.

Material	$f_0$	$s_N$	$\epsilon_N$	$f_N$	$f_{cr}$	$\delta_{GTN}$	$q_1$	$q_2$	$q_3$
Al5182	0.001	0.1	0.270	0.035	0.00213	10	1.5	1.0	2.15
Al5754	0.001	0.1	0.320	0.034	0.00284	7	1.5	1.0	2.15
Al6016	0.001	0.1	0.276	0.036	0.01520	15	1.5	1.0	2.15
Mild steel	0.001	0.1	0.210	0.039	0.0601	5	1.5	1.0	2.15
XES steel	0.001	0.1	0.500	0.040	0.04	5	1.5	1.0	2.15
ULC/Ti	0.001	0.1	0.500	0.040	0.04	5	1.5	1.0	2.15

Figs. 4 and 5 summarize the experimental uniaxial tensile results for the materials taken from Brunet et al. (1998) and Mguil (1997), along with the predictions of the GTN model using the corresponding parameters. All of the stress–strain curves depict the true (Cauchy) stress versus the true (logarithmic) strain. Note that the experimental curves are restricted by the small range of uniform deformation, which is marked by a limit point corresponding to the maximum load, as defined by Considère's criterion. Note also that for the XES and ULC/Ti steels, no experimental tensile results were available in the literature. In order to verify the accuracy of our numerical predictions, the calculations were also performed with the built-in GTN model available in Abaqus/Explicit. As shown in the figures, these simulations coincide with those obtained with the developed UMAT subroutine. Differences between the simulated and experimental curves are observed in some cases, illustrating the difficulty to accurately identify material parameters for constitutive models having a large number of parameters. These discrepancies may also be explained by the material parameters being identified on a small range of strain (i.e., corresponding to the range of uniform elongation of the tensile specimens). Therefore, these sets of material parameters and experimental results are only used for illustration purposes. The aim of the current work is to investigate the correlations between the elastic–plastic–damage model and the localization limits, rather than an in-depth confrontation to experiments. The latter would require accurate parameter identification up to large strains – of the same order of magnitude as the critical localization strains. Instead, we intend to emphasize the impact of these parameters on the predicted limit strains in order to determine the most important ones. This information may prove useful for

setting up accurate identification procedures focusing on the most influential parameters, which is a prerequisite to any proper quantitative comparison with experiments for validation purposes.

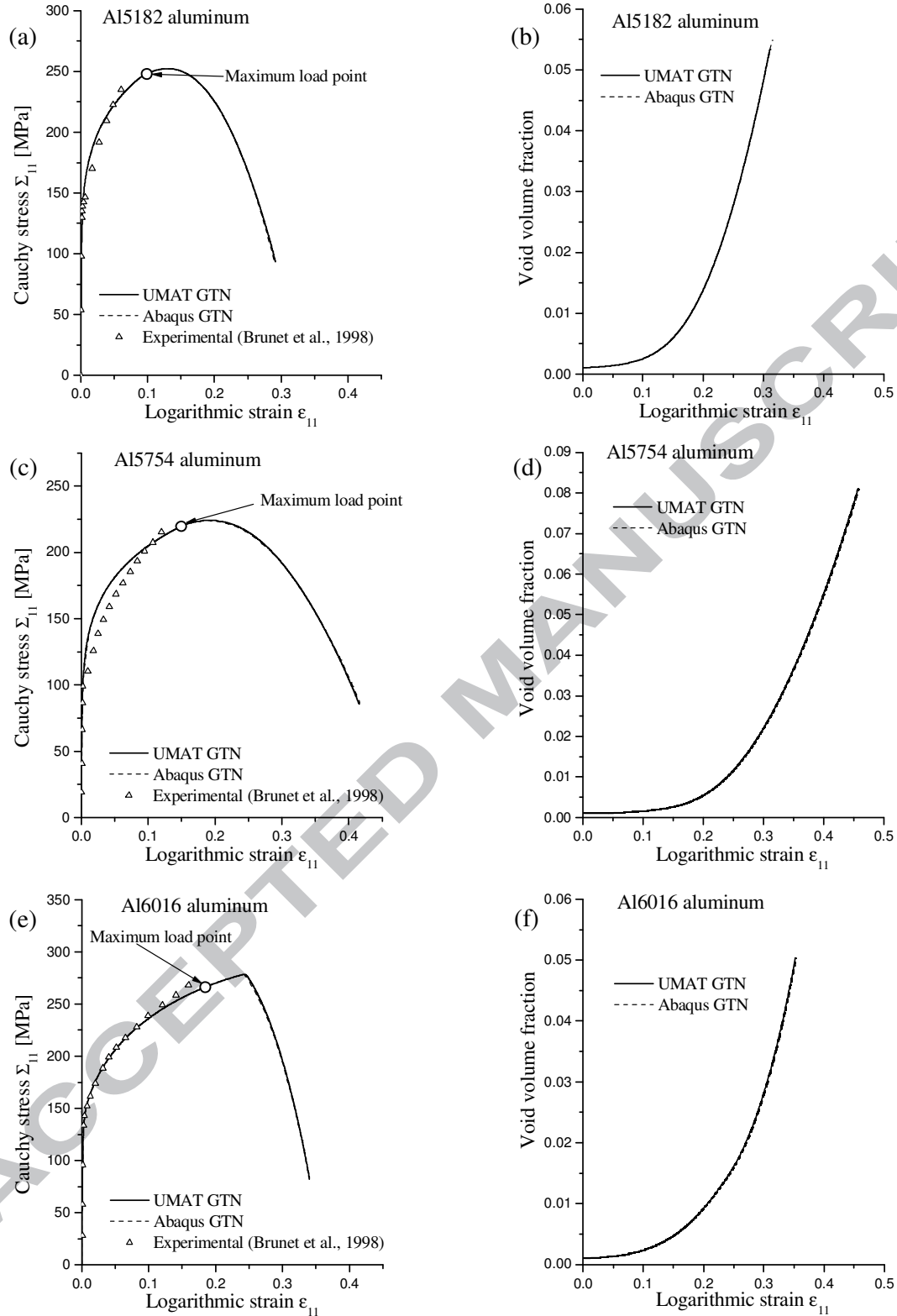


**Fig. 4.** Experimental and numerical uniaxial tensile stress–strain curves (left) and predicted void volume fraction (right) for the three selected aluminum materials: (top) Al5182, (middle) Al5754 and (bottom) Al6016. The material parameters were taken from Brunet et al. (1998).

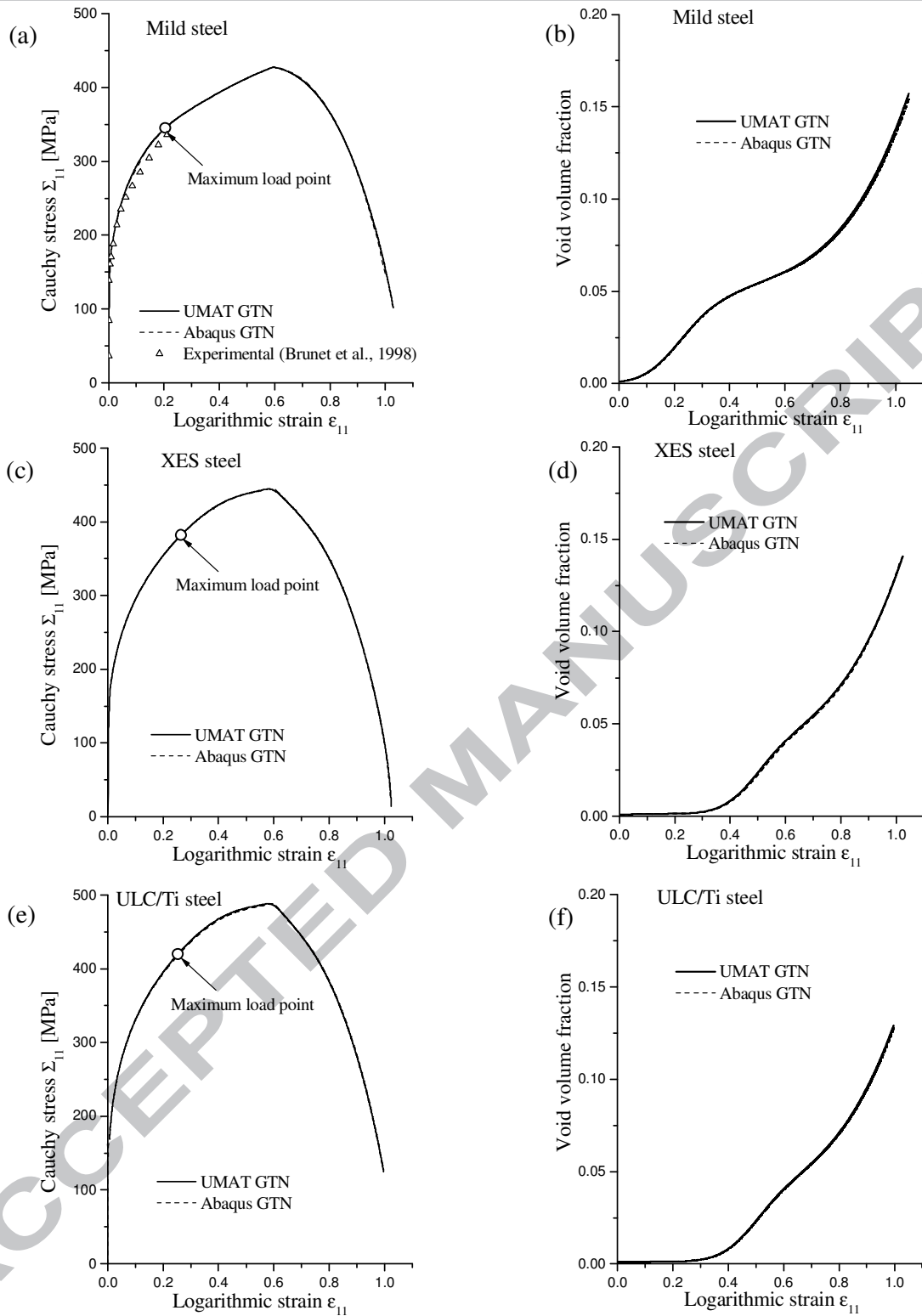


**Fig. 5.** Experimental and numerical uniaxial tensile stress–strain curves (left) and predicted void volume fraction (right) for the three selected steel materials: (top) Mild steel, (middle) XES steel and (bottom) ULC/Ti steel. The material parameters were taken from Brunet et al. (1998) and Mguil (1997).

#### 4.2 Strain localization analysis for typical loading paths

As clarified in the Introduction and in Section 3, the strain localization approach undertaken here is based on a three-dimensional bifurcation analysis from a homogeneous pre-localization state. Such a material instability analysis is usually conducted by imposing all-around displacement boundary conditions so as to rule out geometric instabilities. An element of a solid is thus considered subject to displacement boundary conditions, which in a homogeneous and homogeneously deformed solid would give rise to a uniform deformation field, and conditions are sought under which bifurcation into a localized band mode can occur. This also amounts to considering an infinite block of material, homogeneously deformed through remote loading. In our analysis, this is practically obtained by considering a single finite element, with a single integration point, so as to reproduce various homogeneous stress and strain states until the onset of bifurcation. It is worth noting that in a finite body, structural (geometric) effects, such as diffuse necking, would interrupt this ideal situation of homogeneous deformation before the material instability corresponding to a localized band mode. Consequently, the localization limit strains predicted with an infinite band bifurcation approach are expected to provide an upper bound to those determined experimentally. In the distinct but related context of localized necking in thin metal sheets, Brunet et al. (1998) and Mguil (1997) determined experimental FLDs to which they compared their numerical predictions of limit strains. As previously explained, our three-dimensional bifurcation results are not intended to be quantitatively compared to sheet necking analyses for essentially two reasons. The first is that in the latter case, two-dimensional continua are considered under plane stress conditions, and thus different localization modes are sought. The second reason is that thin metal sheets are finite structures, and as such inherently affected by diffuse necking in experiments. Despite these limitations, an attempt is made to qualitatively compare our bifurcation predictions with the experimentally measured FLDs. To allow for these qualitative comparisons, linear strain paths, inspired from those conventionally applied to in-plane stretched metal sheets in the FLD context, will be remotely prescribed to our infinite block of material. The ductility limits, thus predicted, are represented in terms of curves, referred to as ellipticity loss diagrams (ELDs), which are qualitatively compared in Fig. 6 to the experimental FLDs determined in Brunet et al. (1998) and Mguil (1997). Although qualitative, this comparison is suggestive in several respects. First of all, it can be observed that the difference in terms of overall ductility limit level between aluminum alloys and steels, respectively, is well reproduced. Furthermore, for the steel materials, the developed approach appears as an upper bound with respect to the classical concept of FLDs, as expected from the theory. In particular, for the ULC/Ti steel, the predicted ELD has a shape comparable to that of the experimental FLD. For the aluminum alloys, however, the fact that some of the predicted localization strains fall below their counterparts experimentally measured limit strains seems to corroborate with the observation that the damage evolution was overestimated by a large extent (see the corresponding steep evolution of void volume fraction shown in Figs. 4(b), 4(d) and 4(f) and the associated discussion in subsection 4.1). Inspection of the damage parameters reported in Table 2, suggests that the identified values for the critical porosity of the aluminum alloys are unusually small (e.g., of the order of 0.2% for the Al5182 aluminum alloy), which make it plausible that the damage evolution for the aluminum alloys was overestimated, through identification of premature coalescence initiation. This issue will be further analyzed and discussed in the sequel.

Further assessment of the bifurcation results is possible through analyzing the amount of damage that has developed prior to localization for the different strain paths investigated. The simulations reveal that the plane

strain loading path is the most susceptible to localization, consistent with many theoretical investigations and experiments from the literature (see, e.g., Clausen, 1970; Rice, 1976; Yamamoto, 1978). For illustration, the simulated stress–strain responses until localization are provided in Figs. 7(a) and 7(b) for two materials (Al5182 aluminum and XES steel) and three different strain paths: uniaxial tension (UT), plane strain tension (PST) and balanced biaxial tension (BBT). For the PST loading path, localization is predicted for both materials around the peak of the stress–strain curve, while for UT and BBT strain paths, which are the most resistant to localization, bifurcation is predicted deeper in the softening range. In other words, the value of the critical hardening modulus for localization bifurcation is found close to zero for the PST loading path, while it is strongly negative for the other strain paths represented in the ELDs. These results are consistent with those reported in Yamamoto (1978), where only two loading paths (UT and PST) were investigated (see also, Needleman and Rice, 1978; Saje et al., 1982). Note that in Fig. 7, the end of each stress–strain curve indicates the limit strain associated with localization, as predicted by the singularity of the corresponding acoustic tensor. The evolution of the minimum of the determinant of the acoustic tensor (until its singularity) along each loading path is shown in Figs. 7(c) and 7(d). These results are also consistent with those found by Haddag et al. (2009), who adopted a similar approach that involved the coupling of continuum damage mechanics with Rice’s localization criterion. Another qualitative validation is related to the ductility ratio, defined as the ratio of PST critical strain to UT critical strain. The experiments conducted by Clausen (1970) report a ductility ratio in the range of 0.17 to 0.72 for a variety of steels including mild and high strength steels. The values of the predicted ductility are found in qualitative agreement with those reported in the experiments by Clausen (1970) and Fisher (1980), and the ductility ratio calculated for all of the investigated materials fall in the range experimentally determined by Clausen (1970) and corroborated by subsequent theoretical investigations (see, e.g., Yamamoto, 1978; Needleman and Rice, 1978; Saje et al., 1982).

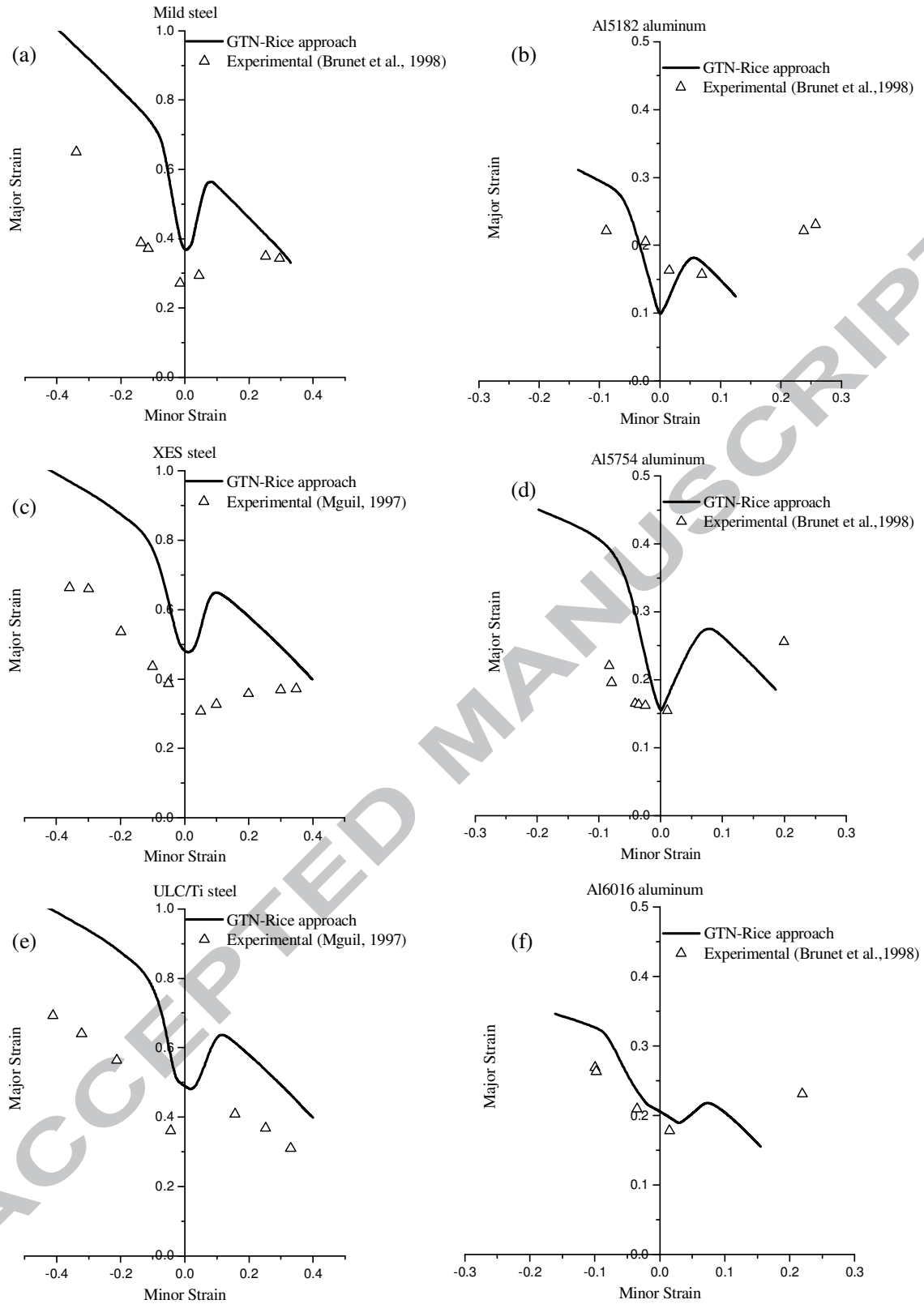


**Fig. 6.** Comparison between the simulated ELDs, predicted by the GTN–Rice bifurcation approach, and the experimental FLDs from Brunet et al. (1998) and Mguil (1997).

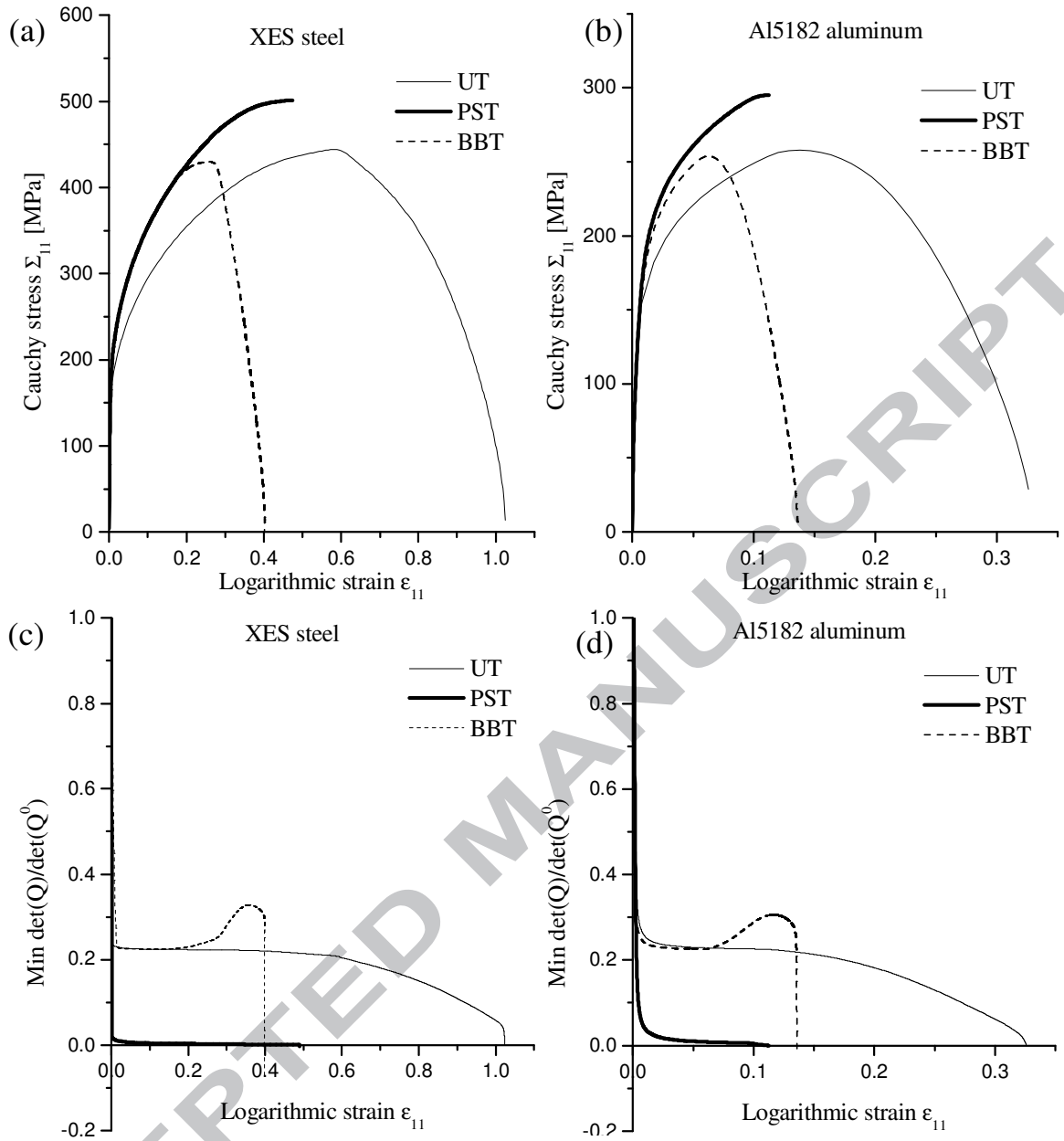


**Fig. 7.** Stress–strain responses until localization for three different loading paths for (a) XES steel and (b) Al5182 aluminum alloy. The evolution of the corresponding minimum of the determinant of the acoustic tensor  $\mathbf{Q}$  is given in (c) and (d), normalized by its elastic value  $\mathbf{Q}^0$ .

A last qualitative check relates to localization along the PST loading path. For this particular strain path, which is very prone to localization, a number of literature results report that localization may be predicted at realistic strain levels, only driven by void growth and/or nucleation. Accordingly, coalescence is not required to occur well before localization for the PST strain path. This has been verified for all of the materials investigated; however, for two aluminum alloys (the Al5182 and Al5754, for which unusually small critical porosities were identified), coalescence is found to initiate much before localization bifurcation, which again corroborate the possibility that the associated damage evolution was overestimated.

### 4.3 Effect of the GTN damage parameters on the limit strain predictions

In this subsection, the effect of the GTN damage parameters on the prediction of ductility limits, depicted in terms of ELDs, is investigated. These parameters are separated into three groups according to the three mechanisms leading to ductile fracture (i.e., nucleation, growth and coalescence). The results of this parameter sensitivity study are obtained by varying one parameter at a time, while the remaining parameters are maintained at a constant level, corresponding to the values in Tables 1 and 2. Each parameter undergoes an increase and a decrease relative to its initial value; the latter intermediate value corresponds to the reference curve associated with the parameters listed in Tables 1 and 2. For conciseness, the results of this investigation are only reported for the XES steel and the Al5182 aluminum alloy.

#### 4.3.1 Effect of the nucleation parameters

Figs. 8(a)–8(f) illustrate the sensitivity of the ductility limits, via the associated ELDs, to the nucleation parameters  $f_N$ ,  $\varepsilon_N$  and  $s_N$ . The impact of parameter  $f_N$  on the ductility limit is shown in Figs. 8(a) and 8(b) for the XES steel and Al5182 aluminum alloy, respectively. Considering the physical significance of this parameter (i.e., the volume fraction of inclusions that are likely to nucleate), it is expected that larger values of parameter  $f_N$  induce rapid damage within the material, thereby promoting early plastic flow localization. This expectation is confirmed by Figs. 8(a) and 8(b), which demonstrate that the predicted ELDs are lowered as parameter  $f_N$  increases. This relationship is also easily understandable when examining Eq. (7), which provides the evolution equation of void nucleation. This equation reveals that  $A_N$ , which controls the nucleation rate, is a monotonously increasing function of parameter  $f_N$ ; thus, larger  $f_N$  values result in faster nucleation.

The impact of parameter  $\varepsilon_N$  on the ductility limit is illustrated in Figs. 8(c) and 8(d). Again, the physical significance of this parameter (i.e., the equivalent plastic strain for which half of the inclusions have nucleated) suggests that larger values of this parameter tend to delay the damage development and, accordingly, the occurrence of material instability. This relationship is also confirmed in Figs. 8(c) and 8(d), which demonstrate that the predicted ELDs are higher as parameter  $\varepsilon_N$  is increased.

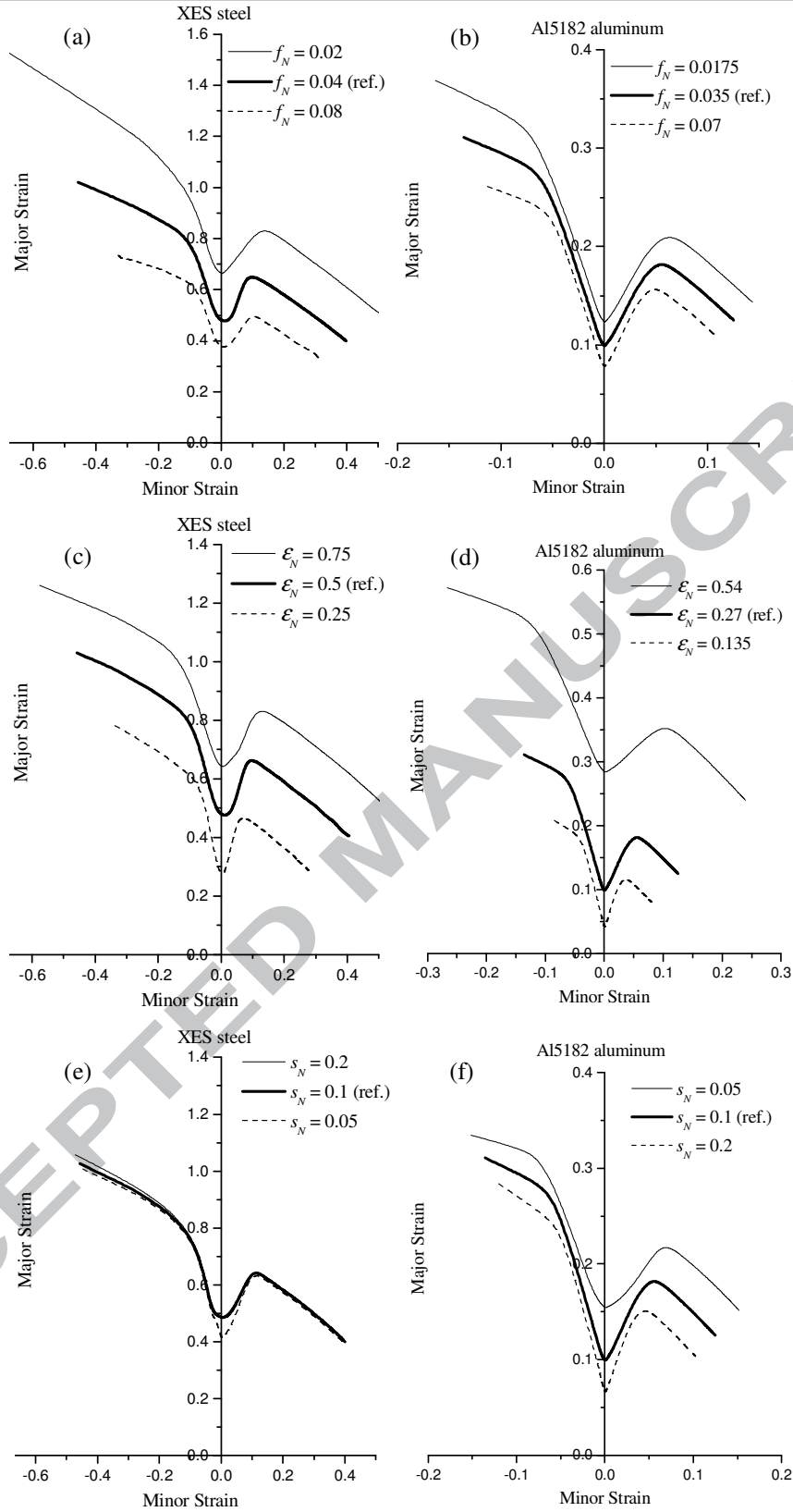


**Fig. 8.** Effect of nucleation parameters on the prediction of the ELDs for the two selected materials: XES steel (left) and Al5182 aluminum alloy (right).

Finally, the impact of the parameter  $s_N$ , which represents the standard deviation on  $\varepsilon_N$ , on the ductility limit is illustrated in Figs. 8(e) and 8(f). First, it can be observed that the effect of  $s_N$  on the Al5182 aluminum alloy is more pronounced than on the XES steel. This fact can be explained as follows: although parameter  $s_N$  undergoes the same variations in both materials, these variations are proportionally larger for the Al5182 aluminum alloy because  $\varepsilon_N$  is smaller for this material (see Table 2). Additionally, it is difficult to expect a general trend for the impact of  $s_N$  on ductility, considering its basic mathematical definition (i.e., standard deviation on  $\varepsilon_N$ ). This preliminary observation is confirmed in Figs. 8(e) and 8(f), which reveal that increasing the parameter  $s_N$  results in a decrease in the ductility of the Al5182 aluminum alloy, while the opposite relationship is observed for the XES steel. Examination of Eq. (7) again indicates that  $A_N$  is not a monotonous function of  $s_N$ , as is also shown from the expression of its derivative with respect to  $s_N$ :

$$\frac{\partial A_N}{\partial s_N} = \frac{f_N}{\sqrt{2\pi}s_N^4} \left[ (\bar{\varepsilon}^p - \varepsilon_N)^2 - s_N^2 \right] \exp \left[ -\frac{1}{2} \left( \frac{\bar{\varepsilon}^p - \varepsilon_N}{s_N} \right)^2 \right].$$

This derivative reveals that  $A_N$  is an increasing function of  $s_N$  for small values of the equivalent plastic strain, while it becomes a decreasing function of  $s_N$  beyond a certain threshold, which depends on the material parameters. Therefore, if plastic flow localization occurs for strain levels that are below this threshold, then larger values of  $s_N$  induce earlier strain localization, whereas the opposite is expected to happen when plastic flow localization occurs for strain levels beyond this threshold.

Figs. 9 and 10 display the corresponding evolution of the Cauchy stress and void volume fraction until localization when the parameters  $f_N$ ,  $\varepsilon_N$  and  $s_N$  are varied for the Al5182 aluminum alloy and XES steel, respectively. Figs. 9(a)–9(d) and 10(a)–10(d) confirm the previously discussed trends for the impact of the parameters  $f_N$  and  $\varepsilon_N$ , which can also be basically interpreted as follows: a faster evolution of void volume fraction tends to promote early strain localization. For parameter  $s_N$ , however, a comparison between Figs. 9(e)–9(f) and Figs. 10(e)–10(f) reveals that, unlike the Al5182 aluminum alloy, there is a strain threshold for the XES steel beyond which the void volume fraction increases more rapidly for smaller values of  $s_N$ . This description completes the above discussion and explains why parameter  $s_N$  appears to reflect an effect on the ductility limit of the XES steel that is the opposite of that of the Al5182 aluminum alloy.

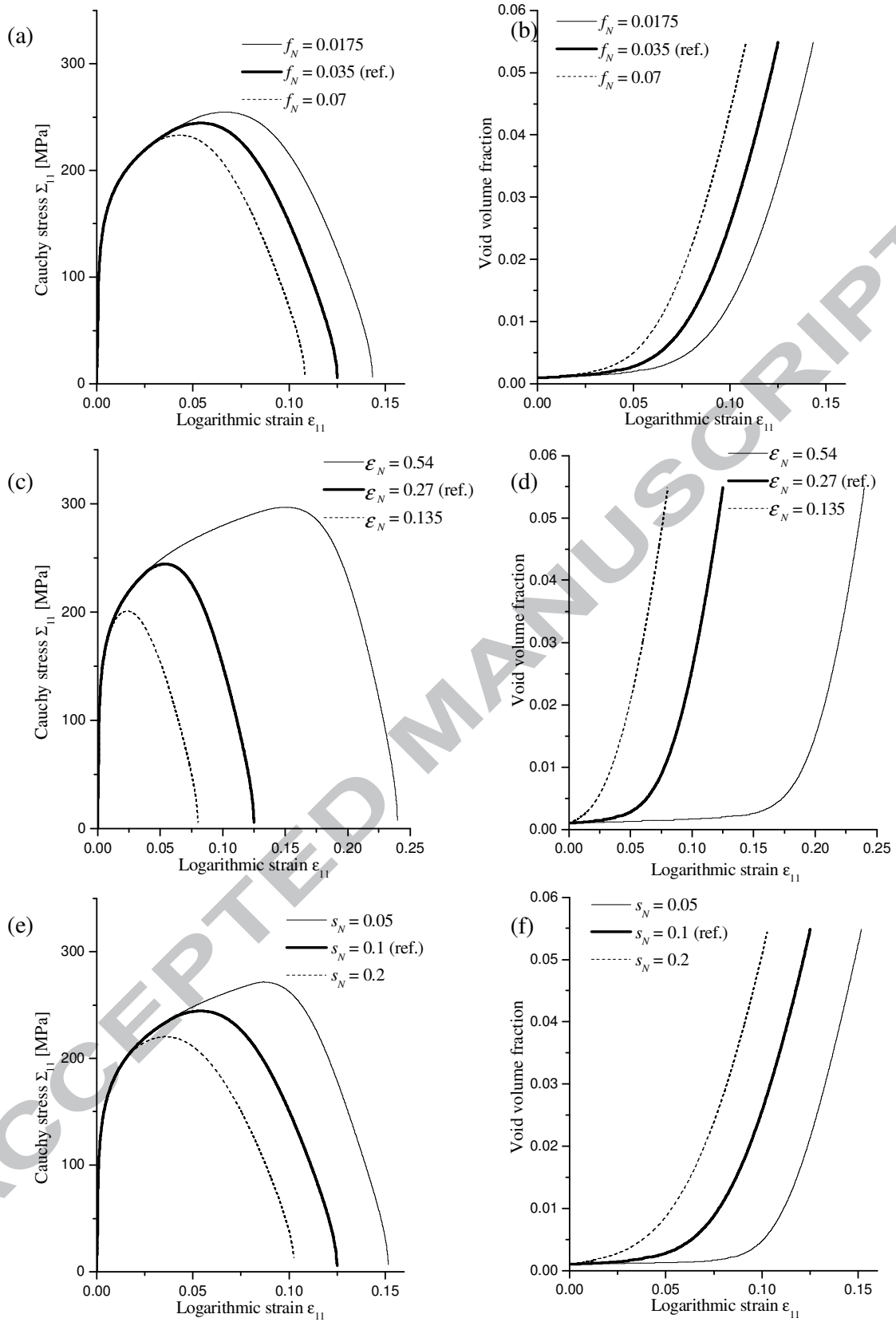


**Fig. 9.** Evolution of the Cauchy stress and void volume fraction until localization along the BBT strain path when parameters  $f_N$ ,  $\epsilon_N$  and  $s_N$  are varied for the Al5182 aluminum alloy.

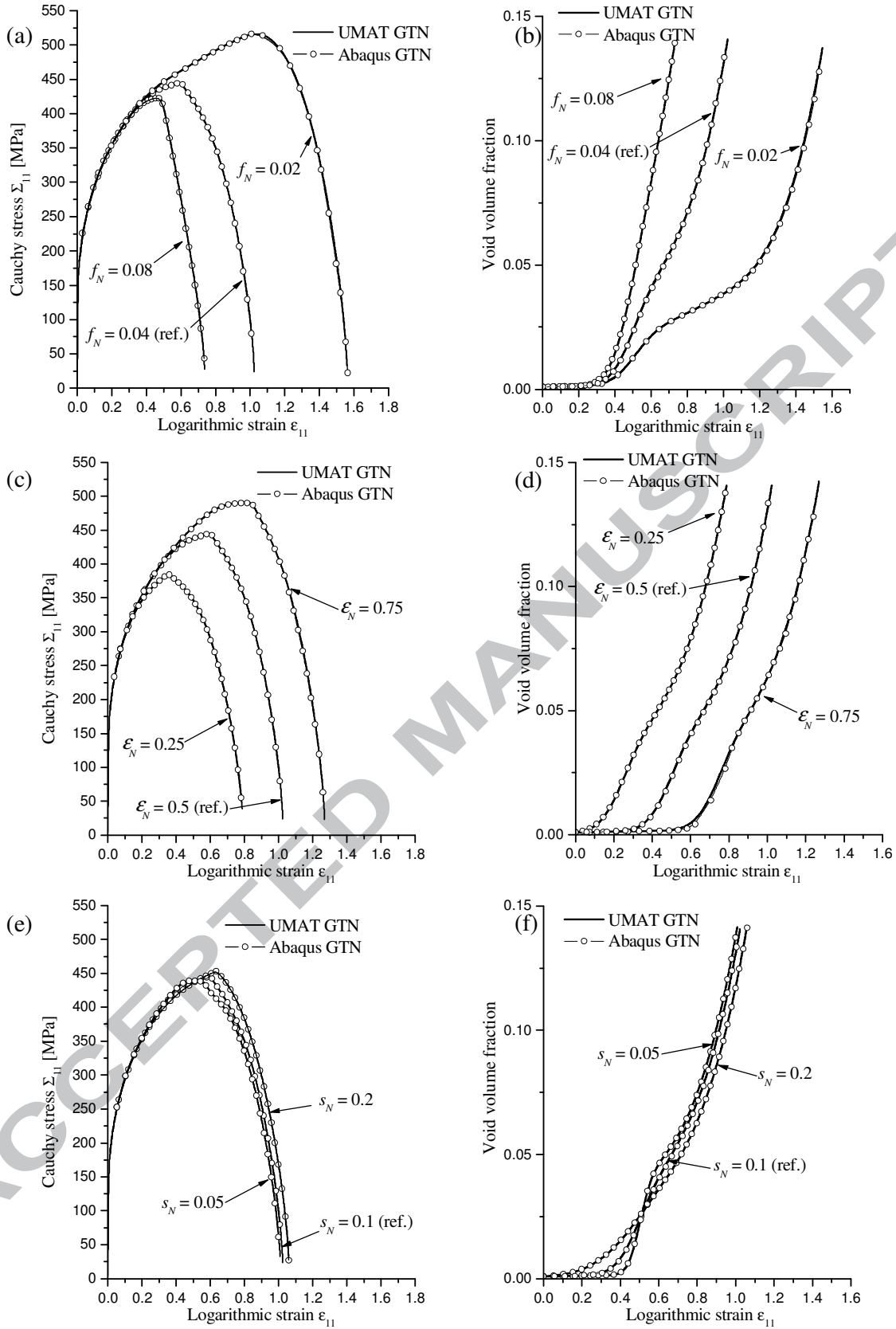


**Fig. 10.** Evolution of the Cauchy stress and void volume fraction until localization along the UT strain path when the parameters  $f_N$ ,  $\epsilon_N$  and  $s_N$  are varied for the XES steel.

Note that all of the simulation results in terms of stress–strain response and void volume fraction evolution were validated with respect to the built-in GTN model available in Abaqus/Explicit (which includes the coalescence phenomenon); some of these validation curves are shown in Fig. 10 for illustration. In particular, some of the stress–strain responses exhibit a sudden change in their slope close to the maximum stress (see, e.g., Figs. 5 and 10). This non-smoothness is correspondingly encountered in plots of the “effective” porosity evolution at the same values of strain, and this corresponds to the start of the coalescence regime, which involves a discontinuity in the “fictitious” effective porosity rate (see Eq. (9)).

A noteworthy observation from the strong impact of the void nucleation parameters on the stress–strain responses (see, e.g., Fig. 9) concerns the closely related issue of material parameter identification. To illustrate this, we restrict attention to one of the void nucleation parameters (e.g.,  $\varepsilon_N$ ) and we report in Fig. 11(a) the corresponding stress–strain responses along with the experimental uniaxial tensile test. Fig. 11(a) shows that, for the selected variations of parameter  $\varepsilon_N$ , the uniaxial stress–strain response is noticeably affected only at moderate or large strains; consequently, identifying the damage parameters using only the small range of uniform elongation of the tensile specimen would result in a non-negligible error on the actual value of  $\varepsilon_N$ . This uncertainty on this parameter value would lead, in turn, to a potential error on the associated ELD (see Fig. 11(b)). Consequently, post-necking investigation of tensile tests (Mirone, 2004; Dunand and Mohr, 2010; Tardif and Kyriakides, 2012), or alternative non-uniform mechanical tests (Haddadi and Belhabib, 2012) must be used to reliably identify these parameters. In this sense, the current parameter sensitivity study could provide useful information for such sample design and parameter identification.

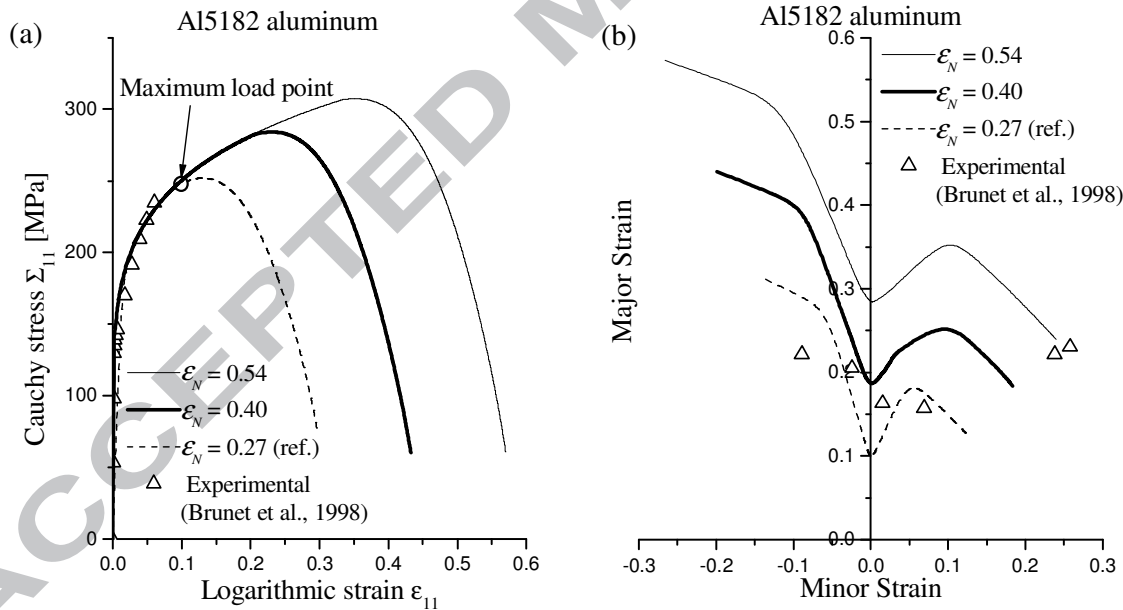


**Fig. 11.** Uniaxial tensile responses (a) and the associated ELDs (b) for the Al5182 aluminum alloy; effect of variation of parameter  $\varepsilon_N$ .

## 4.3.2 Effect of the initial porosity

The initial porosity is one of the key parameters of the Gurson-type damage models (Pardoen and Hutchinson, 2000; Zhang et al., 2000). Because the material void volume fraction increases from this initial value through the mechanisms of nucleation, growth and coalescence, higher values of initial porosity tend to accelerate the damage process, leading to material instability. Figs. 12(a) and 12(b) reflect the sensitivity of the ELDs to the initial porosity for the XES steel and Al5182 aluminum alloy, respectively; as expected, the ELDs are lowered as the parameter  $f_0$  increases. For the largest value of this parameter ( $f_0 = 0.01$ ), the ELD of the Al5182 aluminum alloy is dramatically lowered because, at such a high value, the material has already entered the coalescence stage. One can also observe that for very small initial porosity values, the ELDs are only slightly affected because, in such a range of porosity, nucleation is the dominant mechanism responsible for damage evolution (see Eqs. (6)–(9)). This observation is consistent with the results obtained by Li and Huang (2005), which show that the void growth mechanism is negligible below a critical void size.

Note, however, that the above-predicted destabilizing effect of increasing the initial porosity, although in qualitative agreement with widely reported literature results and experiments, should be somewhat mitigated. Indeed, in the above parameter sensitivity analysis, only one parameter is varied at a time, which does not account for possible mutual influence. In practice, it has been shown that the coalescence parameters, i.e., the critical porosity  $f_{cr}$  and the void volume fraction at final fracture  $f_R$ , depend strongly on the initial porosity  $f_0$  (see, e.g., Becker et al., 1988; Koplik and Needleman, 1988; Zhang and Hauge, 1999). In fact, the critical porosity  $f_{cr}$  increases with increasing the initial porosity, which correspondingly delays the coalescence stage; therefore, the destabilizing effect predicted with an increase in the initial porosity alone should be somehow moderated.

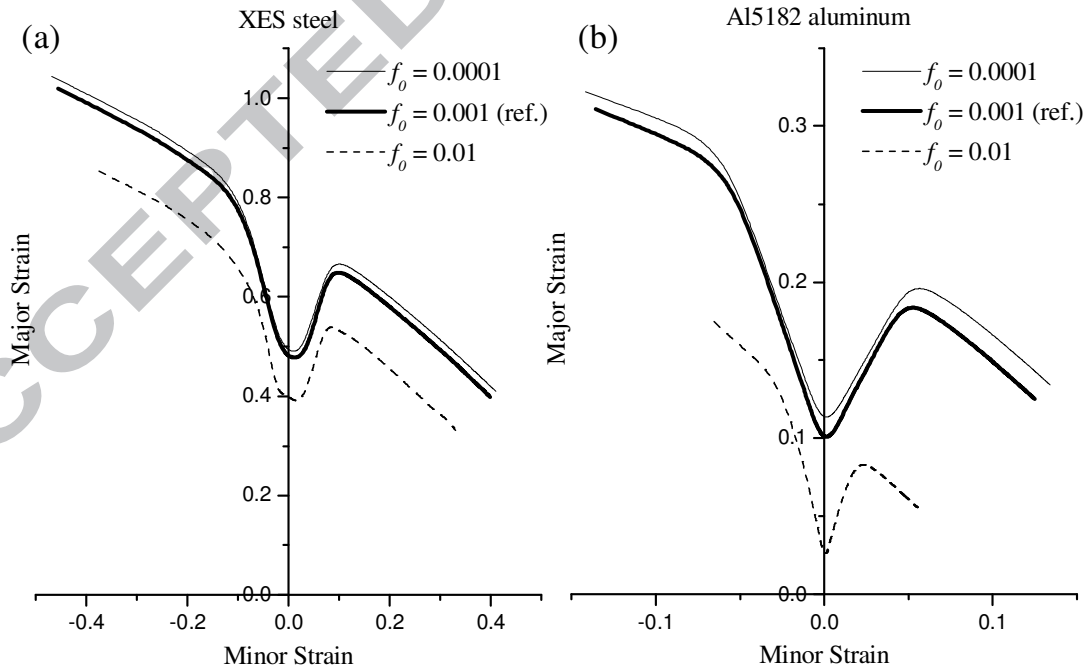


**Fig. 12.** Effect of the initial porosity on the predicted ELDs for the two selected materials: XES steel (left) and Al5182 aluminum alloy (right).

### 4.3.3 Effect of the coalescence parameters

The influence of the parameters that govern the coalescence mechanism on the predicted limit strains is also investigated. Figs. 13(a) and 13(b) reflect the impact of the critical porosity  $f_{cr}$  on the prediction of the ductility limits for the two selected materials. It is found that the ELDs are lowered as parameter  $f_{cr}$  decreases, consistently with the role of this critical porosity that triggers the coalescence regime (see Eq. (9)). With regard to the influence of the ‘acceleration’ term  $\delta_{GTN}$ , Figs. 13(c) and 13(d) show that increasing  $\delta_{GTN}$  tends to reduce the predicted ductility limits. These observed trends are in accordance with the role of this parameter in accelerating the void coalescence and confirm that this phenomenon is a limiting factor for ductility. It can be observed, however, that the predicted PST limit strain is not affected by varying the ‘acceleration’ coalescence parameter  $\delta_{GTN}$  in the case of the XES steel (see Fig. 13(c)), while it is sensibly affected for the Al5182 aluminum alloy (see Fig. 13(d)). This difference is due to the unusually low critical porosity identified for the Al5182 aluminum alloy, resulting in initiation of coalescence along the PST strain path well before localization, as already discussed previously.

The role of the coalescence mechanism is important to underline in several respects. First, this mechanism has been introduced by Tvergaard and Needleman (1984) to allow predicting material failure at realistic values of porosity. In the current work, this mechanism allows us to predict flow localization at realistic strain levels for the full range of loading paths varying from UT to BBT. Recall that earlier investigations, considering only the void growth effect (e.g., Yamamoto, 1978), or combined void growth and nucleation effects (e.g., Saje et al., 1982), predicted localization bifurcation at a realistic strain level only for plane strain tension, and hence had to resort to initial imperfections, analogously to an M–K type analysis.

It is also important to emphasize the significant influence of the coalescence parameters on the predicted limit strains (see Fig. 13), in consideration of its implications for the related issue of material parameter identification. Focusing attention on the ‘acceleration’ parameter, we show in Fig. 14 that the predicted localization point, for UT or BBT strain paths, is located at small (almost vanishing) values of stress for small values of  $\delta_{GTN}$ , while it may be located at larger stress values (up to close to the peak stress) for large values of  $\delta_{GTN}$ . It is noteworthy that values of  $\delta_{GTN}$  as large as 300 have been identified for aluminum alloys (Li et al., 2011).

From the above parameter sensitivity analysis, it clearly appears that the proper identification of the coalescence parameters is a key issue for accurate flow localization predictions. The two independent coalescence parameters in the GTN model are the critical porosity  $f_{cr}$  and the void volume fraction at final fracture  $f_R$ , or equivalently  $f_{cr}$  and  $\delta_{GTN}$ , the latter being inversely proportional to the difference ( $f_R - f_{cr}$ ), (see, Eq. (9)). Early experimental coalescence studies (Brown and Embury, 1973; Goods and Brown, 1979) and numerical model analyses (Andersson, 1977) suggested values of  $f_{cr}$  and  $f_R$  of the order of 0.15 and 0.25, respectively. However, more recent cell model studies (see, e.g., Becker et al., 1988; Koplík and Needleman, 1988) suggest that  $f_{cr}$  and  $f_R$  vary slowly with the dense matrix strain hardening and with the stress triaxiality, but depend strongly on the initial porosity. Such a decrease of  $f_{cr}$  and  $f_R$  with the initial porosity lends support to high values of  $\delta_{GTN}$ , as those recently identified in Li et al. (2011).

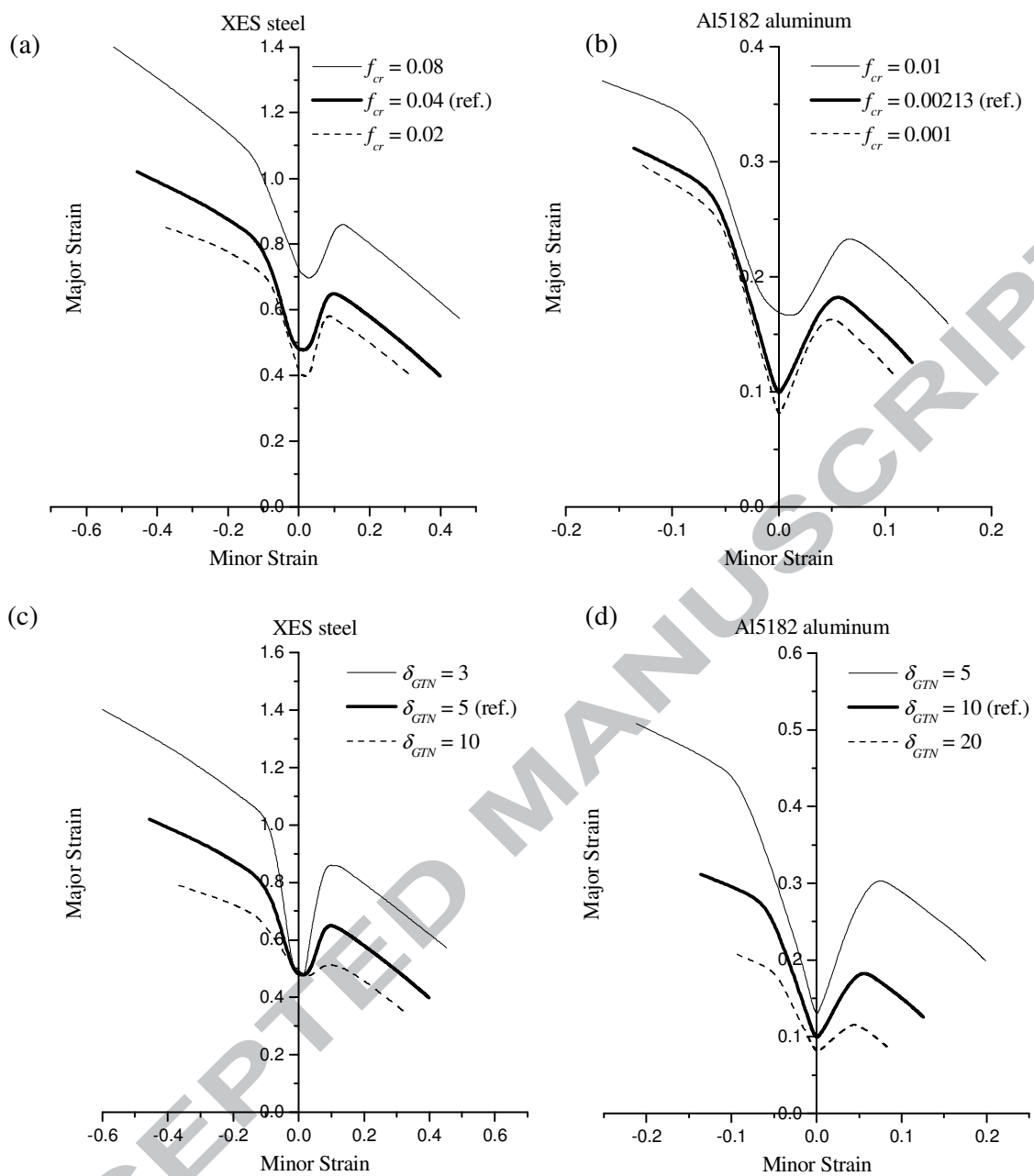


**Fig. 13.** Effect of coalescence parameters on the prediction of the ELDs for the two selected materials: XES steel (left) and Al5182 aluminum alloy (right).

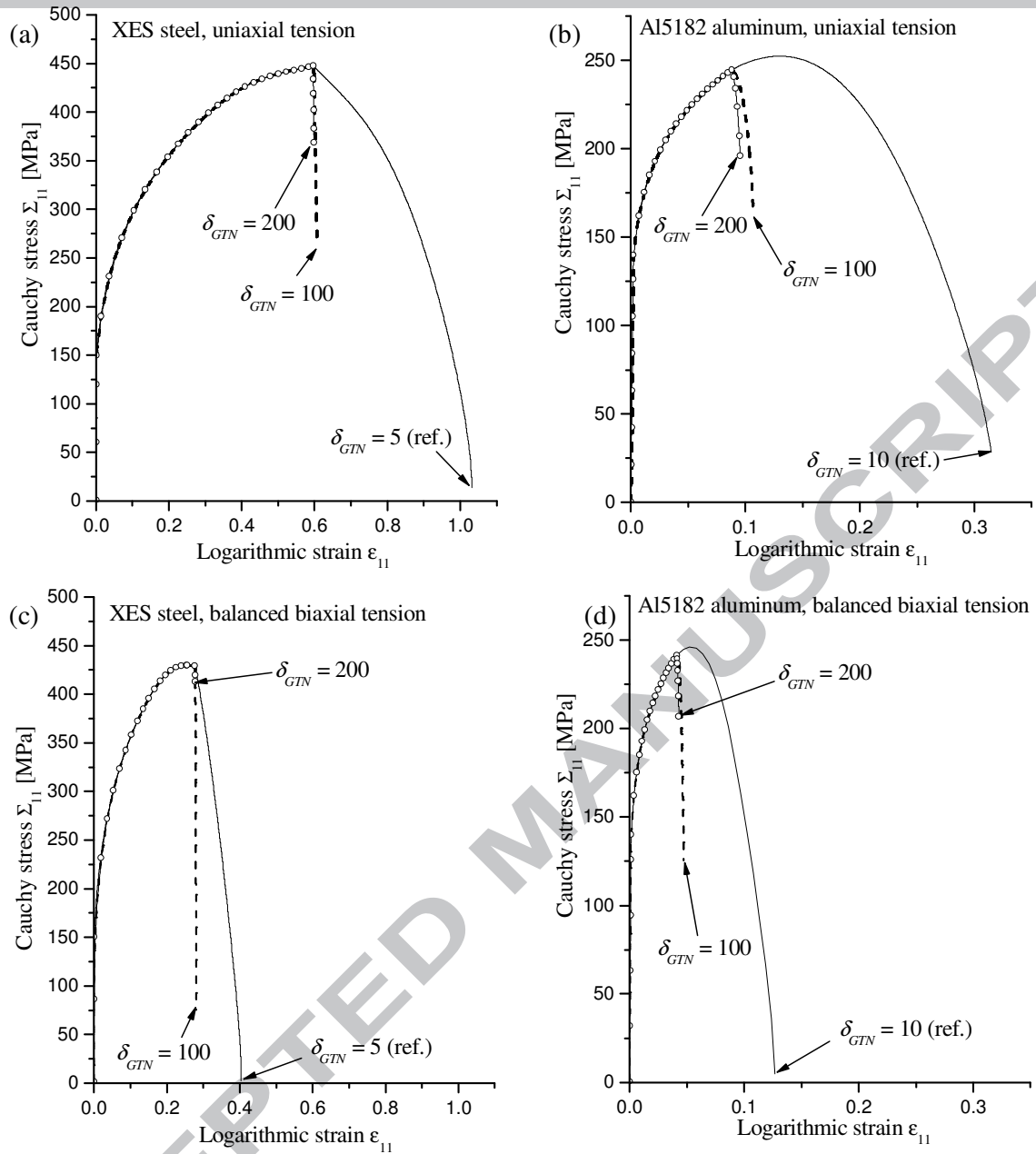


**Fig. 14.** Effect of the ‘acceleration’ factor ( $\delta_{GTN}$ ) on the prediction of strain localization for the XES steel (left) and Al5182 aluminum alloy (right) under uniaxial tension (top) and balanced biaxial tension (bottom).

#### 4.4 Effect of the dense matrix hardening parameters

In this subsection, we investigate the impact on the predicted limit strains of the parameters that govern the strain hardening of the fully dense matrix material. The latter is modeled with the Swift isotropic hardening law, as described by Eq. (2). Fig. 15 shows the influence of the Swift hardening parameters  $k$ ,  $\epsilon_0$  and  $n$  on the predicted ELDs for both selected materials. For the GTN model coupled with the bifurcation approach, the effect of the hardening parameters on the localization predictions appears to be much less significant compared with the impact of the damage-related parameters. This difference may be attributable, in part, to the dominant mechanism in the GTN–Rice coupling, which is the damage-induced softening that

ultimately leads to material instability. However, caution should be taken not to interpret these parameter sensitivity results as: ‘material ductility is insensitive to the material hardening’. Indeed, on the one hand, as pointed out by Needleman and Rice (1978), the hardening parameters in the Gurson model are those of the fully dense matrix material and not of the void–matrix aggregate. And on the other hand, it has been shown that for actual materials (see, e.g., Faleskog et al., 1998), the values of the GTN parameters  $q_1$ ,  $q_2$  and  $q_3$  sensibly depend on the matrix hardening characteristics. Accordingly, in the above sensitivity analysis, appropriate consideration of the dependence of the  $q_i$  values on the hardening characteristics is likely to provide more perceptible effects for the latter. The above-mentioned reservations in the interpretation of the numerical sensitivity analysis to the hardening parameters will be further discussed in what follows.

The above reservations aside, the results in Fig. 15 will be further interpreted using the concept of critical hardening modulus. Unlike the plane strain tension loading path, it has been shown in section 4.2 that most of the loading paths require a strongly negative hardening modulus for localization bifurcation (see also, e.g., Needleman and Rice, 1978). Therefore, because the hardening modulus of the matrix material is positive, only damage-induced softening can bring the effective hardening modulus of the void–matrix aggregate to such negative values. This explains, in part, why for most of the loading paths illustrated in Fig. 15, especially in the extreme parts of the ELDs, varying the dense matrix hardening parameters minimally modifies the predicted limit strains. To complete the explanation, we report in Fig. 16 the evolution of the Cauchy stress and void volume fraction until localization for the Al5182 aluminum alloy along the BBT loading path. In contrast to the impact of the damage parameters previously discussed, Fig. 16 reveals that the porosity evolution is insensitive to the matrix hardening parameters. This issue in the GTN model is due to its original derivation based on an ideal-plastic matrix material. This was pointed out by Leblond et al. (1995), who proposed a modification of the Gurson relation to account for strain hardening effects on void growth rate, while Faleskog et al. (1998) suggested a systematic micromechanics calibration of the  $q_i$  parameters in order for the GTN model to reproduce the observed effects of strain hardening on void growth rate, which were earlier revealed by Tracey (1971).

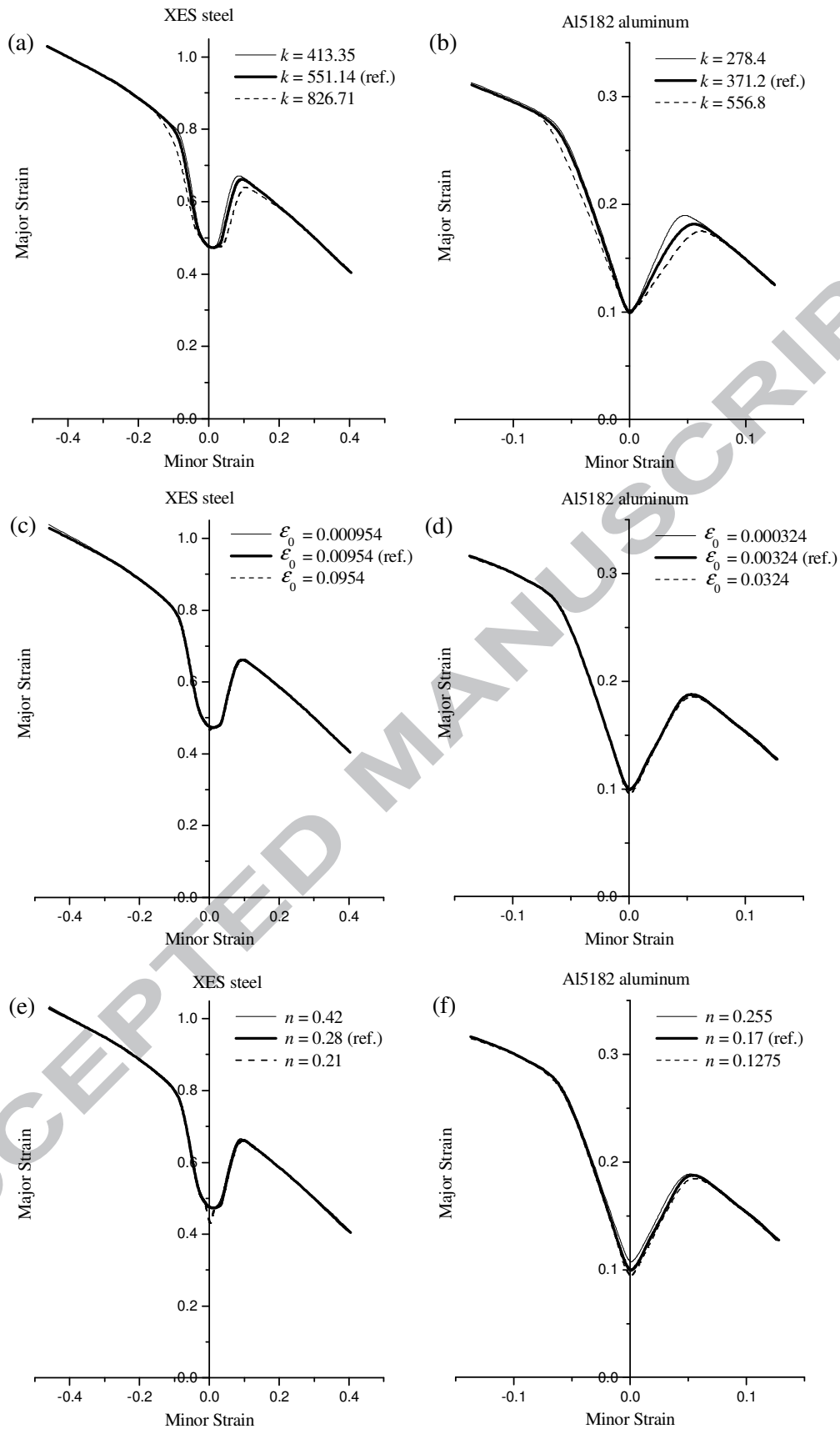


**Fig. 15.** Effect of the dense matrix hardening parameters on the prediction of the ELDs for the two selected materials: XES steel (left) and Al5182 aluminum alloy (right).

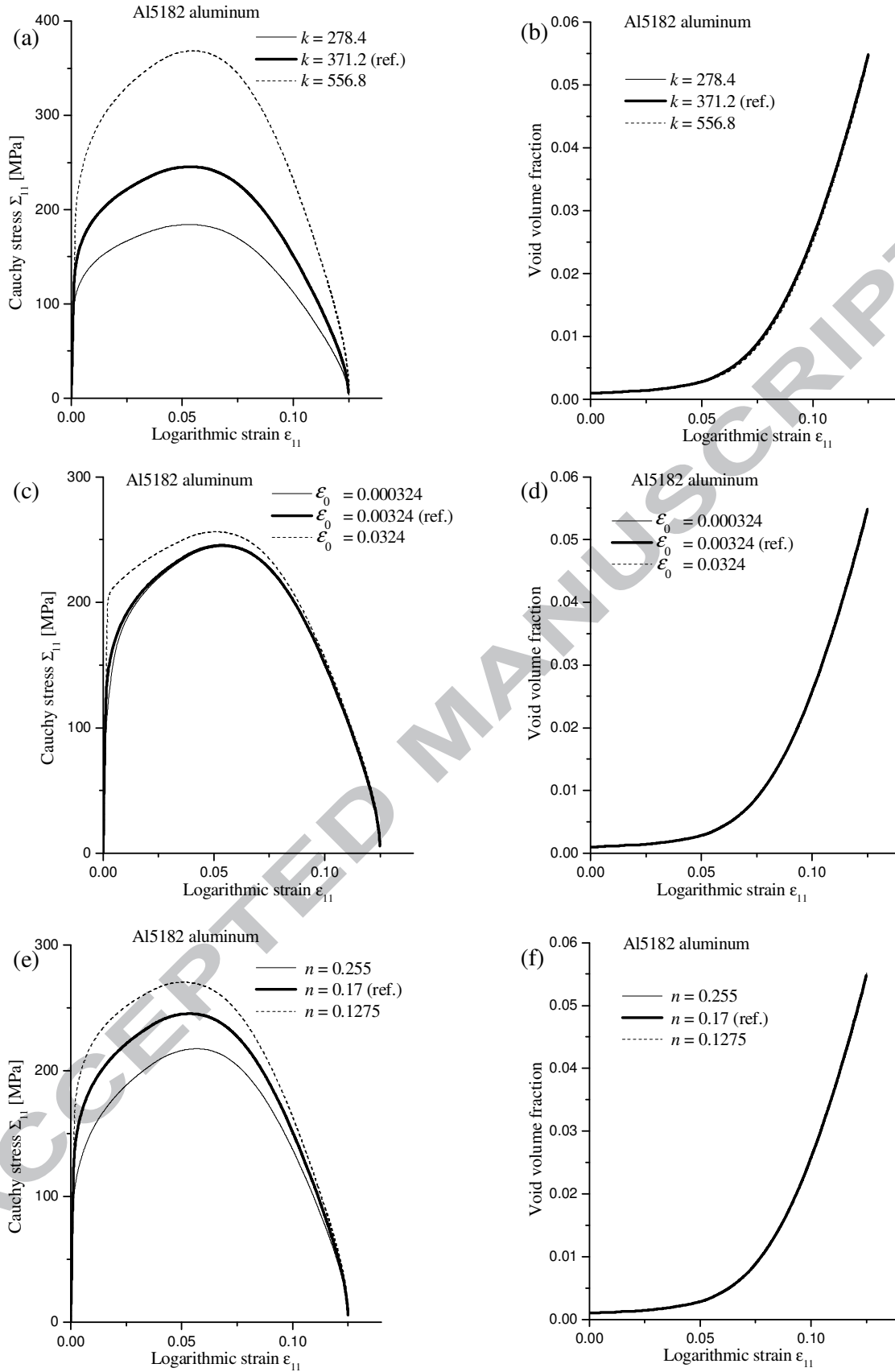


**Fig. 16.** Evolution of the Cauchy stress and void volume fraction until localization along the BBT strain path when the parameters  $k$ ,  $\epsilon_0$  and  $n$  are varied for the Al5182 aluminum alloy.

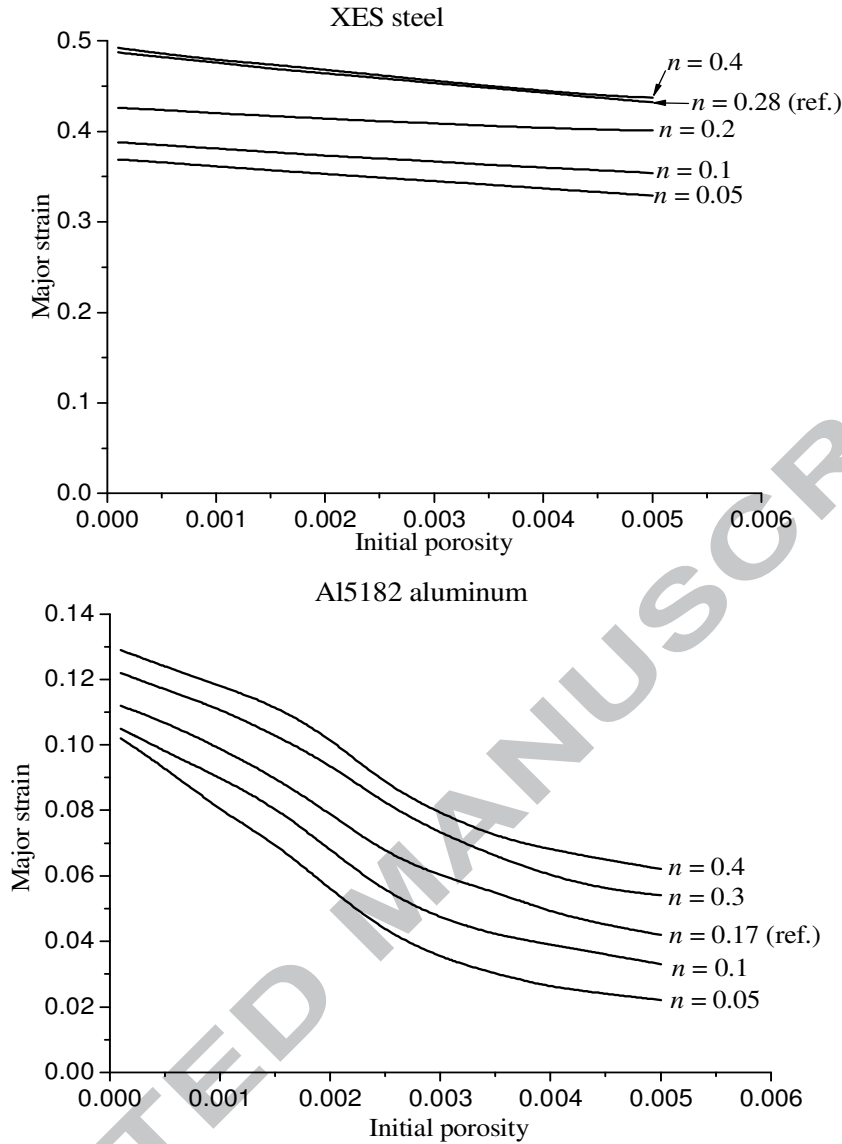


**Fig. 17.** Evolution of the critical localization strain (for the PST strain path) with the initial porosity for different values of the dense matrix hardening coefficient  $n$  : (top) XES steel, (bottom) Al5182 aluminum alloy.

For the plane strain tension loading path, which is the most susceptible to flow localization, as it requires a critical hardening modulus close to zero, the effect of the hardening parameters is more perceptible (see Figs. 15(e) and 15(f)). To highlight this effect, another representation is provided in Fig. 17, where the evolution of the critical localization strain with the initial porosity is plotted for different values of the dense matrix hardening coefficient  $n$ . As expected, Fig. 17 better emphasizes the effect of parameter  $n$  for the PST strain path, with the PST critical strain increasing with the hardening coefficient  $n$ . It is noteworthy that for this strain path, localization is predicted at smaller porosity, and thus for such small values of void volume fraction, the matrix hardening characteristics should be more representative of those of the void–matrix aggregate. These results are consistent with those reported in Yamamoto (1978), where the original Gurson model restricted to the void growth effect was applied only for the plane strain tension loading path, while we extend here the bifurcation analysis to the modified GTN model including the void nucleation and

coalescence mechanisms and enlarge the investigation to the full range of loading paths varying from UT to BBT.

Another qualitative validation concerns the ductility ratio (i.e., ratio of PST critical strain to UT critical strain) for different values of the hardening exponent  $n$ . This ratio is found to increase with increasing  $n$ , for all studied materials, consistent with previous model analyses (see, e.g., Yamamoto, 1978; Needleman and Rice, 1978; Saje et al., 1982) and experiments (see, Clausing, 1970); moreover, this ductility ratio is found to fall in the range revealed by the above literature studies, and to follow the observed trend that it is the PST ductility, rather than the UT ductility, which is most affected by variations in the hardening characteristics.

In the distinct but related context of localized necking in thin metal sheets, several investigations have addressed the effect of strain hardening on material formability, mostly by means of the maximum-force-based criteria. These criteria were originally designed to predict diffuse necking, as proposed by Swift (1952), and then specifically extended to be able to predict localized necking, which occurs after diffuse necking has developed (Hora et al., (1996)). For example, for a rigid–plastic von Mises constitutive model that considers Hollomon’s isotropic hardening law, the limit strains based on Swift’s and Hora’s criteria under plane stress conditions are directly proportional to the hardening coefficient  $n$ . This shows that hardening has a non-negligible impact on the formability limits predicted with these maximum-force-based criteria when combined with simple constitutive equations (e.g., rigid-plasticity with isotropic hardening and no coupling with damage). The imperfection-based formability prediction approach proposed by Marciniak and Kuczynski (1967) is also sensitive to the hardening parameters, as shown in several studies (e.g., Zhao et al., 1996). Even predictions based on bifurcation theory have been shown to be sensitive to hardening in the context of localized necking in thin metal sheets (see, e.g., Stören and Rice, 1975; Doghri and Billardon, 1995). In Stören and Rice (1975), the use of a finite-strain version of the  $J_2$  deformation theory of plasticity, which introduces yield surface vertex effects, makes it possible to predict bifurcation in the range of positive hardening moduli, where strain hardening plays a non-negligible role. In Doghri and Billardon (1995), however, damage-induced softening is required for bifurcation along certain strain paths; nevertheless, within the adopted continuum damage mechanics framework with strong coupling (see, e.g., Lemaitre, 1992), the hardening characteristics do affect the evolution of damage.

To summarize, for the current GTN constitutive model coupled with bifurcation theory, it appears that strain localization is essentially controlled by the damage-induced softening and the corresponding parameters. As a practical implication of this parametric study, the precise identification of the GTN damage parameters seems to be a prerequisite for accurate strain localization analyses based on Rice’s bifurcation criterion.

#### 4.5 *Effects of prestrain and of convective stress components*

In this subsection, we analyze the effects on the prediction of strain localization of a prestrain and of the so-called convective stress terms, respectively. Note that these convective stress terms originate from the large-strain framework (see Eqs. (26)–(30)) and enter the expression of the tangent modulus  $\mathbf{L}$  in Eq. (31), on which the expression of the acoustic tensor is based. When these terms are omitted, the tangent modulus  $\mathbf{L}$  is reduced to the analytical elastic–plastic tangent modulus in Eq. (16). For certain metallic materials, these convective stress terms are small in magnitude compared with the elasticity tensor, and it seems then reasonable to expect that their effect on flow localization predictions may be small (e.g., when the ratio of the

initial yield stress to the Young modulus is of the order of  $10^{-3}$  or less). For the two selected materials, the ductility predictions are provided in Fig. 18, showing the effects of a prestrain and of the convective stress terms, respectively.

For the influence of a prestrain on the predicted ELDs, two different types of prestrain are considered, namely a 10% uniaxial tensile prestrain and a 5% balanced biaxial tensile prestrain. The ELDs obtained by application of linear strain paths without prestrain are called ‘direct ELDs’ and shown in Figs. 18(a) and 18(b), while those obtained after prestrain are referred to as ‘sequential ELDs’ and reported in Figs. 18(c) and 18(d). These results reveal that, with respect to the direct ELDs, the sequential ELDs are translated to the left, for uniaxial tensile prestrain, while they are translated to the right, for balanced biaxial tensile prestrain. These predictions are in accordance with previously reported results, related either to three-dimensional flow localization analyses (see, e.g., Franz et al., 2009b; Haddag et al., 2009), or pertaining to plane stress localized necking studies in the context of thin metal sheets (see, e.g., Stoughton and Zhu, 2004; Stoughton and Yoon, 2011).

With regard to the convective stress components, Fig. 18 reveals that their effect on the predicted ELDs is negligibly small for both studied materials and both loading conditions (i.e., with and without prestrain). Therefore, these results suggest that the use of the analytical elastic–plastic tangent modulus, with no convective stress terms, is sufficient for analyzing the ductility limits of the investigated materials without loss of accuracy. This simplifying assumption is often made in the literature; the above-discussed results represent a numerical verification of validity of such an assumption. In relation with the concept of critical hardening modulus, the results above are also consistent with those of Rudnicki and Rice (1975), who developed the critical hardening modulus in terms of an expansion in the stress/elastic modulus ratio, showing that neglecting the convective stress components amounts to restricting this expansion to the zero-th order term. For most of the strain paths investigated, localization bifurcation requires a strongly negative hardening modulus, which is essentially characterized by the zero-th order term in the expansion, and hence the above simplifying assumption is fully justified. However, when the zero-th order term in the critical hardening modulus expansion is itself small, as in the case of plane strain tension where it is around zero, the convective stress components may have some non-negligible effect.

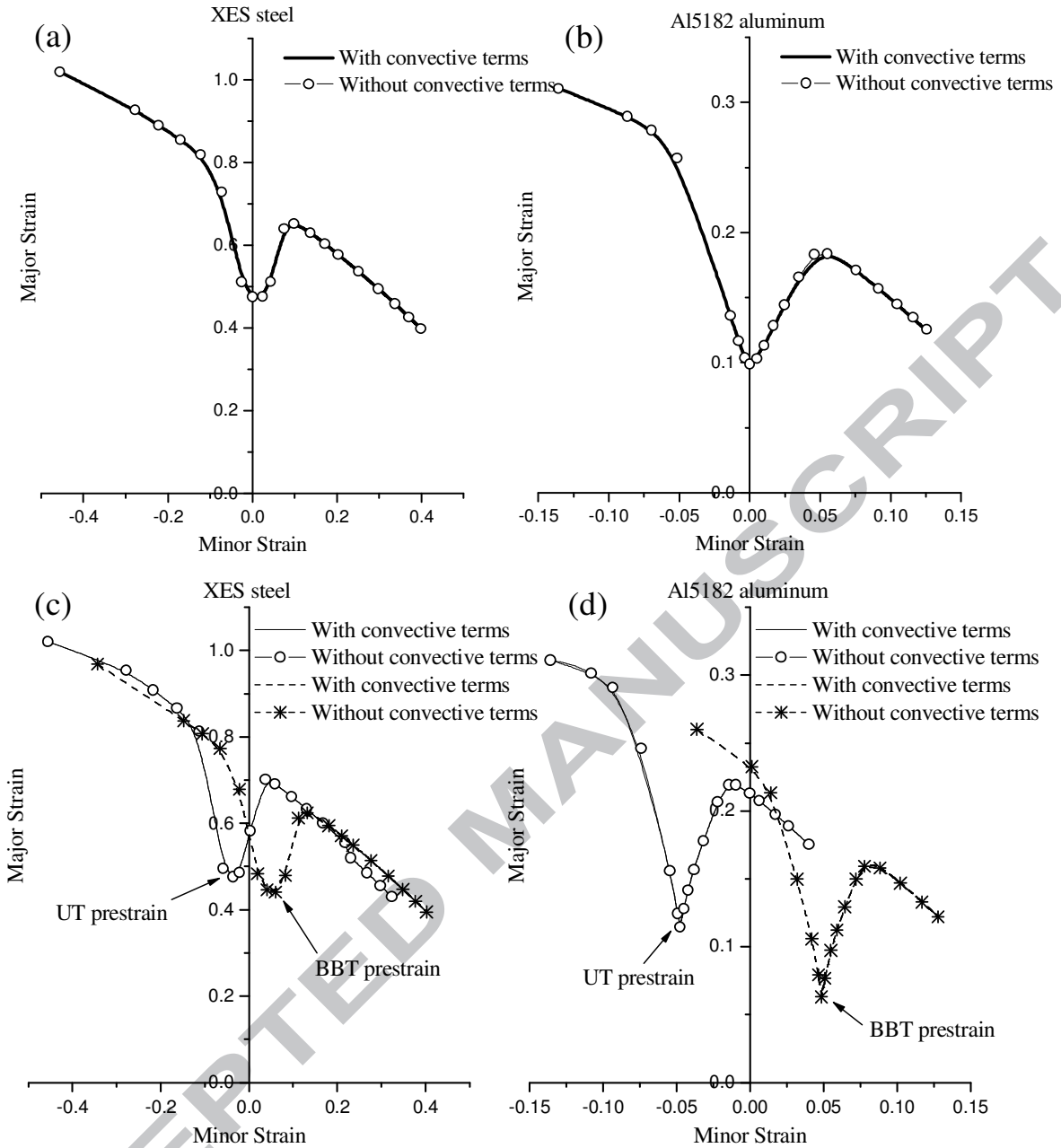


**Fig. 18.** Effects of the convective stress terms and of a prestrain (10% uniaxial tensile prestrain and 5% balanced biaxial tensile prestrain) on the prediction of the ELDs for the two selected materials: XES steel (left) and Al5182 aluminum alloy (right).

## 5. Concluding remarks and discussion

In this study, the GTN elastic–plastic–damage modeling has been combined with the Rice localization criterion, which is based on bifurcation theory, to investigate the localization of deformation into narrow planar bands. The resulting coupling, with governing equations derived within a large-strain, fully three-dimensional framework, has been implemented into the static implicit FE code Abaqus/Standard. This approach is then applied to the prediction of ductility, set by plastic flow localization, for a representative selection of ductile materials taken from the literature. The corresponding ductility limit predictions,

associated with linear strain paths typical of those applied to metals under in-plane biaxial stretching, are represented in terms of ellipticity loss diagrams and discussed in some details with respect to previously reported literature results and experiments.

The current work parallels and enlarges the earlier investigation by Yamamoto (1978) where, by considering only the mechanism of void growth in the original Gurson model, it was found that it is necessary to introduce some form of initial imperfection to predict localization strains at a realistic level. Several subsequent contributions extended the analysis to include various effects, such as void nucleation, strain-rate sensitivity, yield surface curvature, while still restricting the analysis to the growth of initial imperfections and only particular strain paths, such as plane strain tension or axisymmetric uniaxial tension. In the current analysis, however, by accounting for all mechanisms of growth, nucleation, and coalescence, within the GTN damage model, localization bifurcation is predicted at realistic strain levels for the full range of strain paths varying from UT to BBT. Also, the associated ductility limits are found in qualitative agreement with literature results and experiments.

A sensitivity analysis, with respect to the material parameters, was then conducted on two selected materials, an Al5182 aluminum alloy and an XES steel, to identify the most influential parameters on the ductility limit predictions. These parameters were divided into several groups to disclose their respective impacts on strain localization and to discuss their effects based on physical or mathematical considerations. The obtained results were in accordance with the physical interpretation of the GTN parameters. The damage-related parameters were shown to have a significant impact on the predicted limit strains. In contrast, the dense matrix hardening parameters had much smaller effects on the prediction of the limit strains with this bifurcation approach compared with the predominant role played by the damage parameters. These general trends are attributable, in part, to the dominant mechanism in the GTN–Rice modeling, which is the damage-induced softening that ultimately leads to the material instability. However, caution should be taken in interpreting the numerical sensitivity analysis with respect to the hardening parameters, as the latter pertain to the fully dense matrix material and not to the void–matrix aggregate. In addition, the actual influence of material hardening on ductility should be more consistently undertaken within an improved version of the GTN model that accounts for the strain hardening effect on void growth rate (see, e.g., Leblond et al., 1995), or by appropriate consideration of the dependence of the  $q_i$  values on the matrix hardening characteristics (see, e.g., Faleskog et al., 1998).

For the PST strain path, which is very prone to strain localization, the effect of hardening has been found to be more noticeable, consistent with previously reported literature results. This is explained by inspecting the critical hardening modulus required for bifurcation, which is close to zero for the particular PST strain path, while it is found to be strongly negative for the other strain paths investigated. Several features or mechanisms, not considered in the current analysis, are likely to bring the critical hardening modulus to higher levels, which in turn would bring some of the localization sensitivity predictions more in line with commonly observed trends. One of the most influential aspects is related to the initial imperfections (i.e., geometric or materials inhomogeneities), inherently present in actual materials, which significantly reduce the predicted limit strains as compared to the bifurcation approach (Yamamoto, 1978). Similar features that promote flow localization are expected from the introduction of a yield surface vertex or non-normality in the plastic flow (Rudnicki and Rice, 1975). With this regard, the use of stress-controlled rather than strain-controlled nucleation leads to non-normality along with its corresponding well-known destabilizing role

(Needleman and Rice, 1978). Also, the consideration of kinematic hardening, and the associated effect on yield surface curvature, has been shown to precipitate earlier flow localization (Mear and Hutchinson, 1985; Tvergaard, 1987). Not to mention the deleterious effect of diffuse necking, which has been approximately taken into account in Saje et al. (1982), showing a noticeable decrease in the predicted limit strains, due to the resulting increase in stress triaxiality. Which of these mechanisms, or which combination of factors, will bring the model predictions into closer agreement with physical or experimental observations would require more in-depth investigations.

Note also that there are secondary benefits to this parametric study. In particular, determining the most influential material parameters may contribute to direct attention towards a smaller set of parameters both in terms of more refined physical modeling and precise parameter identification. For example, for the GTN constitutive model, it appears that localization bifurcation is essentially controlled by the damage evolution law and the corresponding parameters. As a practical implication, the precise evaluation of the GTN damage parameters seems to be a prerequisite for the accurate strain localization analyses based on Rice's bifurcation criterion. Furthermore, based on the physical interpretation of certain material parameters, the proposed prediction tool may be used advantageously to help design new materials with enhanced ductility and in-use properties (see, e.g., Zhao et al., 2008; Kobayashi, 2010; Shanthraj and Zikry, 2012).

For further qualitative validation, the prestrain effect on the predicted limit strains was also analyzed. The well-known trends of uniaxial tensile prestrain and balanced biaxial tensile prestrain were consistently confirmed. Finally, the role of the convective stress components, arising from the large-strain framework, in the prediction of the limit strains was investigated. For the two selected materials and for both loading conditions (i.e., linear and sequential strain paths), the convective stress terms were shown to have little effect on the predicted localization strains. These results suggest that the use of the analytical elastic–plastic tangent modulus alone is sufficient for analyzing the limit strains of certain materials (e.g., when the corresponding convective stress terms are small in magnitude compared with the elasticity tensor). This property, once fully validated, may be advantageously used to determine efficient strategies that can be applied to the minimization of the determinant of the acoustic tensor, based on a consideration of its symmetry.

## References

- Andersson, H., 1977. Analysis for a model for void growth and coalescence ahead of a moving crack tip. *Journal of the Mechanics and Physics of Solids* 25, 217–233.
- Becker, R., 2011. An alternative approach to integrating plasticity relations. *International Journal of Plasticity* 27, 1224–1238.
- Becker, R., Needleman, A., Richmond, O., Tvergaard, V., 1988. Void growth and failure in notched bars. *Journal of the Mechanics and Physics of Solids* 36, 317–351.
- Benallal, A., 1998. Three-dimensional analysis of localized necking. In: R. De Borst, E. van der Giessen (Eds.), *Material instabilities in solids*. John Wiley & Sons Ltd., pp. 255–268.
- Benzerga, A.A., Besson, J., 2001. Plastic potentials for anisotropic porous solids. *European Journal of Mechanics – A/Solids* 20, 397–434.
- Benzerga, A.A., Besson, J., Pineau, A., 2004a. Anisotropic ductile fracture – I. Experiments. *Acta Materialia* 52, 4623–4638.
- Benzerga, A.A., Besson, J., Pineau, A., 2004b. Anisotropic ductile fracture – II. Theory. *Acta Materialia* 52, 4639–4650.

- Besson, J., Guillemer-Neel, C., 2003. An extension of the Green and Gurson models to kinematic hardening. *Mechanics of Materials* 35, 1–18.
- Besson, J., Steglich, D., Brocks, W., 2003. Modeling of plane strain ductile rupture. *International Journal of Plasticity* 19, 1517–1541.
- Bigoni, D., Hueckel, T., 1991. Uniqueness and localization – I. Associative and non-associative elastoplasticity. *International Journal of Solids and Structures* 28, 197–213.
- Borg, U., 2007. Strain gradient crystal plasticity effects on flow localization. *International Journal of Plasticity* 23, 1400–1416.
- Brown, L.M., Embury, J.D., 1973. The initiation and growth of voids at second phase particles. In: *Proc. 3rd Int. Conf. on Strength of Metals and Alloys*. Institute of Metals, London, pp. 164–169.
- Brunet, M., Mguil, S., Morestin, F., 1998. Analytical and experimental studies of necking in sheet metal forming processes. *Journal of Materials Processing Technology* 80-81, 40–46.
- Brüning, M., 2002. Numerical analysis and elastic-plastic deformation behavior of anisotropically damaged solids. *International Journal of Plasticity* 18, 1237–1270.
- Brüning, M., 2003. An anisotropic ductile damage model based on irreversible thermodynamics. *International Journal of Plasticity* 19, 1679–1713.
- Chu, C., Needleman, A., 1980. Void nucleation effects in biaxially stretched sheets. *Journal of Engineering Materials and Technology* 102, 249–256.
- Clausing, D.P., 1970. Effect of plastic strain state on ductility and toughness. *International Journal of Fracture Mechanics* 6, 71–85.
- Considère, A., 1885. Mémoire sur l'emploi du fer et de l'acier dans les constructions. *Ann. Ponts et Chaussées* 9, 574–775.
- Doghri, I., Billardon, R., 1995. Investigation of localization due to damage in elasto-plastic materials. *Mechanics of Materials* 19, 129–149.
- Dunand, M., Mohr, D., 2010. Hybrid experimental-numerical analysis of basic ductile fracture experiments for sheet metals. *International Journal of Solids and Structures* 47, 1130–1143.
- Drucker, D., 1956. On uniqueness in the theory of plasticity. *Quarterly of Applied Mathematics* 14, 35–42.
- Faleskog, J., Gao, X., Shih, C.F., 1998. Cell model for nonlinear fracture analysis – I. Micromechanics calibration. *International Journal of Fracture* 89, 355–373.
- Fisher, J.R., 1980. Void nucleation in spheroidized steels during tensile deformation. Ph.D. Thesis, Brown University.
- Franz, G., Abed-Meraim, F., Ben Zineb, T., Lemoine, X., Berveiller, M., 2009a. Strain localization analysis using a multiscale model. *Computational Materials Science* 45, 768–773.
- Franz, G., Abed-Meraim, F., Lorrain, J.P., Ben Zineb, T., Lemoine, X., Berveiller, M., 2009b. Ellipticity loss analysis for tangent moduli deduced from a large strain elastic–plastic self-consistent model. *International Journal of Plasticity* 25, 205–238.
- Gologanu, M., Leblond, J.B., Perrin, G., Devaux, J., 1997. Recent extensions of Gurson's model for porous ductile metals. In: P. Suquet, *Continuum Micromechanics, CISM Courses and Lectures*. New York: Springer, pp. 61–130.
- Goods, S.H., Brown, L.M., 1979. The nucleation of cavities by plastic deformation. *Acta Metallurgica* 27, 1–15.
- Goodwin, G., 1968. Application of strain analysis to sheet metal forming problems in the press shop. SAE Technical Paper No. 680093.
- Gurson, A.L., 1977. Continuum theory of ductile rupture by void nucleation and growth: Part I – yield criteria and flow rules for porous ductile media. *Journal of Engineering Materials and Technology* 99, 2–15.
- Haddadi, H., Belhabib, S., 2012. Improving the characterization of a hardening law using digital image correlation over an enhanced heterogeneous tensile test. *International Journal of Mechanical Sciences* 62, 47–56.

- Haddag, B., Abed-Meraim, F., Balan, T., 2009. Strain localization analysis using a large deformation anisotropic elastic–plastic model coupled with damage. *International Journal of Plasticity* 25, 1970–1996.
- Haddag, B., Balan, T., Abed-Meraim, F., 2007. Investigation of advanced strain-path dependent material models for sheet metal forming simulations. *International Journal of Plasticity* 23, 951–979.
- Hill, R., 1952. On discontinuous plastic states, with special reference to localized necking in thin sheets. *Journal of the Mechanics and Physics of Solids* 1, 19–30.
- Hill, R., 1958. A general theory of uniqueness and stability in elastic–plastic solids. *Journal of the Mechanics and Physics of Solids* 6, 236–249.
- Hill, R., 1962. Acceleration waves in solids. *Journal of the Mechanics and Physics of Solids* 10, 1–16.
- Hora, P., Tong, L., Reissner, J., 1996. A prediction method of ductile sheet metal failure in FE simulation. *Numisheet*, 252–256. Michigan USA.
- Hutchinson, J., 1979. Survey of some recent work on the mechanics of necking. In: R.E. Kelly (Ed.), *Proceedings of the Eighth U.S. National Congress of Applied Mechanics*. North Hollywood, California: Western Periodicals Co., pp. 87–98.
- Hutchinson, J.W., Neale, K.W., 1978. Sheet Necking – II. Time-independent behavior. In: D.P. Koistinen, N.M. Wang (Eds.), *Mechanics of sheet metal forming*. New York: Plenum Press, pp. 127–153.
- Hutchinson, J.W., Neale, K.W., Needleman, A., 1978. Sheet Necking – I. Validity of plane stress assumptions of the long-wavelength approximation. In: D.P. Koistinen, N.M. Wang (Eds.), *Mechanics of sheet metal forming*. New York: Plenum Press, pp. 111–126.
- Ito, K., Satoh, K., Goya, M., Yoshida, T., 2000. Prediction of limit strain in sheet metal-forming processes by 3D analysis of localized necking. *International Journal of Mechanical Sciences* 42, 2233–2248.
- Jeong, H.Y., Pan, J., 1992. The effects of rate sensitivity and plastic potential surface curvature on plastic flow localization in porous solids. *International Journal of Fracture* 56, 317–332.
- Keeler, S., Backofen, W.A., 1963. Plastic instability and fracture in sheets stretched over rigid punches. *ASM Transactions Quarterly* 56, 25–48.
- Kim, J.H., Lee, M.-G., Barlat, F., Wagoner, R.H., Chung, K., 2008. An elasto-plastic constitutive model with plastic strain rate potentials for anisotropic cubic metals. *International Journal of Plasticity* 24, 2298–2334.
- Kobayashi, M., 2010. Analysis of deformation localization based on proposed theory of ultrasonic wave velocity propagating in plastically deformed solids. *International Journal of Plasticity* 26, 107–125.
- Koplik, J., Needleman, A., 1988. Void growth and coalescence in porous plastic solids. *International Journal of Solids and Structures* 24, 835–853.
- Leblond, J.B., Perrin, G., Devaux, J., 1995. An improved Gurson-type model for hardenable ductile metals. *European Journal of Mechanics – A/Solids* 14, 499–527.
- Lecarme, L., Tekoglu, C., Pardoën, T., 2011. Void growth and coalescence in ductile solids with stage III and stage IV strain hardening. *International Journal of Plasticity* 27, 1203–1223.
- Lee, B., Mear, M., 1990. Effect of inclusion shape on the stiffness of nonlinear two-phase composites. *Journal of the Mechanics and Physics of Solids* 39, 627–649.
- Lele, S.P., Anand, L., 2009. A large-deformation strain-gradient theory for isotropic viscoplastic materials. *International Journal of Plasticity* 25, 420–453.
- Lemaitre, J., 1992. *A course on damage mechanics*. Berlin: Springer.
- Li, H.X., Buckley, C.P., 2010. Necking in glassy polymers: Effects of intrinsic anisotropy and structural evolution kinetics in their viscoplastic flow. *International Journal of Plasticity* 26, 1726–1745.
- Li, H., Fu, M.W., Lu, J., Yang, H., 2011. Ductile fracture: Experiments and computations. *International Journal of Plasticity* 27, 147–180.
- Li, Y., Karr, D.G., 2009. Prediction of ductile fracture in tension by bifurcation, localization, and imperfection analyses. *International Journal of Plasticity* 25, 1128–1153.

- Li, Z., Huang, M., 2005. Combined effects of void shape and void size – oblate spheroidal microvoid embedded in infinite non-linear solid. *International Journal of Plasticity* 21, 625–650.
- Loret, B., Rizzi, E., 1997a. Anisotropic stiffness degradation triggers the onset of strain localization. *International Journal of Plasticity* 13, 447–459.
- Loret, B., Rizzi, E., 1997b. Qualitative analysis of strain localization. Part II: Transversely isotropic elasticity and plasticity. *International Journal of Plasticity* 13, 501–519.
- Marciniak, Z., Kuczynski, K., 1967. Limit strains in the process of stretch forming sheet metal. *International Journal of Mechanical Sciences* 9, 609–620.
- Mattiasson, K., Sigvant, M., Larson, M., 2006. Methods for forming limit prediction in ductile metal sheets. In: Santos, A.D., Barata da Rocha, A. (Eds.), *Proc. IDDRG'06. Porto*, pp. 1–9.
- Mear, M.E., Hutchinson, J.W., 1985. Influence of yield surface curvature on flow localization in dilatant plasticity. *Mechanics of Materials* 4, 395–407.
- Menzel, A., Ekh, M., Runesson, K., Steinmann, P., 2005. A framework for multiplicative elastoplasticity with kinematic hardening coupled to anisotropic damage. *International Journal of Plasticity* 21, 397–434.
- Mirone, G., 2004. A new model for the elastoplastic characterization and stress–strain determination on the necking section of a tensile specimen. *International Journal of Solids and Structures* 41, 3545–3564.
- Mguil, S., 1997. Une technique de corrélation directe d'images numériques : application à la détermination de courbes limites de formage et proposition d'un critère de striction. Ph.D. Thesis, Villeurbanne, Institut National des Sciences Appliquées de Lyon.
- Monchiet, V., Cazacu, O., Charkaluk, E., Kondo, D., 2008. Macroscopic yield criteria for plastic anisotropic materials containing spheroidal voids. *International Journal of Plasticity* 24, 1158–1189.
- Mroginski, J.L., Etse, G., Vrech, S.M., 2011. A thermodynamical gradient theory for deformation and strain localization of porous media. *International Journal of Plasticity* 27, 620–634.
- Needleman, A., Rice, J.R., 1978. Limits to ductility set by plastic flow localization. In: D.P. Koistinen, N.M. Wang (Eds.), *Mechanics of sheet metal forming*. New York: Plenum Press, pp. 237–267.
- Needleman, A., Tvergaard, V., 1977. Necking of biaxially stretched elastic–plastic circular plates. *Journal of the Mechanics and Physics of Solids* 25, 159–183.
- Neilsen, M.K., Schreyer, H.L., 1993. Bifurcations in elastic–plastic materials. *International Journal of Solids and Structures* 30, 521–544.
- Pan, J., Saje, M., Needleman, A., 1983. Localization of deformation in rate sensitive porous plastic solids. *International Journal of Fracture* 21, 261–278.
- Pardoen, T., Hutchinson, J.W., 2000. An extended model for void growth and coalescence. *Journal of the Mechanics and Physics of Solids* 48, 2467–2512.
- Petryk, H., Thermann, K., 1996. Post-critical plastic deformation of biaxially stretched sheets. *International Journal of Solids and Structures* 33, 689–705.
- Rice, J.R., 1976. The localization of plastic deformation. *Theoretical and Applied Mechanics*. Koiter ed., 207–227.
- Rice, J.R., Tracey, D.M., 1969. On the ductile enlargement of voids in triaxial stress fields. *Journal of the Mechanics and Physics of Solids* 17, 201–217.
- Rizzi, E., Loret, B., 1997. Qualitative analysis of strain localization. Part I: Transversely isotropic elasticity and isotropic plasticity. *International Journal of Plasticity* 13, 461–499.
- Rudnicki, J.W., Rice, J.R., 1975. Conditions for the localization of deformation in pressure sensitive dilatant materials. *Journal of the Mechanics and Physics of Solids* 23, 371–394.
- Saje, M., Pan, J., Needleman, A., 1982. Void nucleation effects on shear localization in porous plastic solids. *International Journal of Fracture* 19, 163–182.
- Sánchez, P.J., Huespe, A.E., Oliver, J., 2008. On some topics for the numerical simulation of ductile fracture. *International Journal of Plasticity* 24, 1008–1038.

- Shanthraj, P., Zikry, M.A., 2012. Dislocation-density mechanisms for void interactions in crystalline materials. *International Journal of Plasticity* 34, 154–163.
- Stören, S., Rice, J.R., 1975. Localized necking in thin sheets. *Journal of the Mechanics and Physics of Solids* 23, 421–441.
- Stoughton, T.B., Yoon, J.W., 2011. A new approach for failure criterion for sheet metals. *International Journal of Plasticity* 27, 440–459.
- Stoughton, T.B., Zhu, X., 2004. Review of theoretical models of the strain-based FLD and their relevance to the stress-based FLD. *International Journal of Plasticity* 20, 1463–1486.
- Sun, X., Choi, K.S., Liu, W.N., Khaleel, M.A., 2009. Predicting failure modes and ductility of dual phase steels using plastic strain localization. *International Journal of Plasticity* 25, 1888–1909.
- Swift, H.W., 1952. Plastic instability under plane stress. *Journal of the Mechanics and Physics of Solids* 1, 1–18.
- Tardif, N., Kyriakides, S., 2012. Determination of anisotropy and material hardening for aluminum sheet metal. *International Journal of Solids and Structures* 49, 3496–3506.
- Tekoglu, C., Pardoen, T., 2010. A micromechanics based damage model for composite materials. *International Journal of Plasticity* 26, 549–569.
- Tracey, D.M., 1971. Strain-hardening and interaction effects on the growth of voids in ductile fracture. *Engineering Fracture Mechanics* 3, 301–315.
- Tvergaard, V., 1981. Influence of voids on shear band instabilities under plane strain conditions. *International Journal of Fracture* 17, 389–407.
- Tvergaard, V., 1982. Material failure by void coalescence in localized shear bands. *International Journal of Solids and Structures* 18, 659–672.
- Tvergaard, V., 1987. Effect of yield surface curvature and void nucleation on plastic flow localization. *Journal of the Mechanics and Physics of Solids* 35, 43–60.
- Tvergaard, V., 1993. Necking in tensile bars with rectangular cross-section. *Computer Methods in Applied Mechanics and Engineering* 103, 273–290.
- Tvergaard, V., Needleman, A., 1984. Analysis of the cup-cone fracture in a round tensile bar. *Acta Metallurgica* 32, 157–169.
- Valanis, K.C., 1989. Banding and stability in plastic materials. *Acta Mechanica* 79, 113–141.
- Voyiadjis, G., Kattan, P., 1999. *Advances in Damage Mechanics: Metals and Metal Matrix Composites*. Oxford, UK: Elsevier.
- Wu, P.D., Lloyd, D.J., Jain, M., Neale K.W., Huang, Y., 2007. Effects of spatial grain orientation distribution and initial surface topography on sheet metal necking. *International Journal of Plasticity* 23, 1084–1104.
- Xu, X.P., Needleman, A., 1992. The influence of nucleation criterion on shear localization in rate-sensitive porous plastic solids. *International Journal of Plasticity* 8, 315–330.
- Yamamoto, H., 1978. Conditions for shear localization in the ductile fracture of void-containing materials. *International Journal of Fracture* 14, 347–365.
- Zhang, F., Bower, A.F., Mishra, R.K., Boyle, K.P., 2009. Numerical simulations of necking during tensile deformation of aluminum single crystals. *International Journal of Plasticity* 25, 49–69.
- Zhang, Z., Hauge, H., 1999. On the Gurson micro-mechanical parameters. In: Panotín, T., Sheppard, S. (Eds.), *Fatigue and Fracture Mechanics: Twenty-Ninth Volume*. ASTM STP 1332, pp. 364–383.
- Zhang, Z.L., Thaulow, C., Ødegård, J., 2000. A complete Gurson model approach for ductile fracture. *Engineering Fracture Mechanics* 67, 155–168.
- Zhao, L., Sowerby, R., Sklad, M.P., 1996. A theoretical and experimental investigation of limit strains in sheet metal forming. *International Journal of Mechanical Sciences* 38, 1307–1317.
- Zhao, Z., Ramesh, M., Raabe, D., Cuitino, A.M., Radovitzky, R., 2008. Investigation of three-dimensional aspects of grain-scale plastic surface deformation of an aluminum oligocrystal. *International Journal of Plasticity* 24, 2278–2297.

**Research highlights**

- A large-strain elastic–plastic–damage GTN model is coupled with the Rice bifurcation theory.
- The resulting GTN–Rice coupling is used to predict ductility limits set by plastic flow localization.
- A sensitivity analysis with respect to model parameters is conducted on selected ductile materials.
- The role of softening in triggering plastic flow localization is shown predominant in this approach.
- The proper identification of damage parameters has a significant impact on the model predictions.

ACCEPTED MANUSCRIPT